On the Nature of Sodium Excess in Nearby Galaxies

Borislav Nedelchev

submitted to the University of Hertfordshire in partial fulfilment of the
requirements of the degree of MSc by Research

March 2016

Abstract

The $5890, 5895\text{Å}$ Na D absorption lines are sometimes found to be strongly enhanced in nearby galaxies, compared to what is predicted by the best-fitting models for the stellar continuum. The resulting Na D absorption excess could be caused either by intrinsically stronger absorption feature in the stellar continuum, due to stellar-population effects that are unaccounted by current population synthesis models, interstellar absorption or both. Using the sample of Jeong et al. (2013) and modelling the excess Na D absorption by means of physically motivated line-profile we derived the kinematics of such an excess absorption. Further drawing from the properties of the host galaxies we address the origin of such an enhanced Na absorption. In the galaxies, where no ionised-gas emission is detected and no reddening by dust is present, the Na D spectral profile is observed to be broader than the stellar line-of-sight velocity distribution, suggesting that most likely in these galaxies the Na D excess arise from stellar photospheric absorption. Conversely, objects with an Na D excess profile narrower than the stellar photospheric lines and exhibiting some reddening by dust have also a small red shift associated to their kinematics, a behaviour that can be explained in terms of interstellar absorption occurring in dust lanes that are not always perfectly settled. In objects with a strong reddening by dust and ionised-gas emission, indicating the presence of a considerable interstellar medium, we can find Na D excess profiles that are clearly blue-shifted, an indication for outflowing cold-gas. In our sample, we found that the objects, hosting outflows, are most likely generally, showing features of intense star-formation activity, or are with nebular emission, powered by a mix of star-forming and nuclear activity, with the latter sometimes attributed to accretion onto a supermassive black hole. Per se, the presence of an active galactic nucleus was found not to be relevant in driving such outflows.

Table of contents

List of figures

List of tables

Chapter 1

Introduction

Under the Lambda Cold Dark Matter (ΛCDM) paradigm structure at different scales forms hierarchically - starting from smaller astronomical objects and subsequently assembling into larger cosmological structures. Soon after the Big Bang dark matter clumped around primordial density fluctuations and formed progressively denser regions as the Universe expanded in size and cooled down. Such dark matter clumps then merged into larger structures providing the necessary gravitational potential wells for the baryonic gas to collapse into stars and further assemble into galaxies (White & Rees 1978). Computer simulations, implementing such a gravitational scenario, complemented with the underlying baryonic physics, have been largely successful in explaining many of the observed properties of galaxies over an extensive range of time- and length-scales, such as the power spectrum of the large scale structure, the so-called 'cosmic web', and to some extent the normalization and shape of the galaxy luminosity function (Croton et al. 2006; Genel et al. 2014).

In this context, large-scale gaseous outflows are thought to play an important role in the evolution and formation of galaxies in the Universe (Veilleux et al. 2005). Such outflows, either driven by intense star-formation (Erb 2015) or active galactic nuclei (Everett 2007), have often been invoked to consolidate the results from large-scale structure simulations and observation (Croton et al. 2006). It is now widely accepted that star-formation-driven feedback provides the necessary means to account for the discrepancy between observation and computer models at the low-luminosity end of the galaxy luminosity function. However, at the bright end of the luminosity function, massive galaxies retain their gas more efficiently, facilitating more star formation, resulting in an increase in mass, luminosity, and 'blue' galaxy colour at odds with observations. Indeed, the star-burst feedback effect towards suppressing star formation in this case is only temporary, proven not to be energetic enough to drive the gas out of the gravitational potential well enough, as to quench a great fraction of any potential star-formation (Benson et al. 2003; Puchwein & Springel 2013).
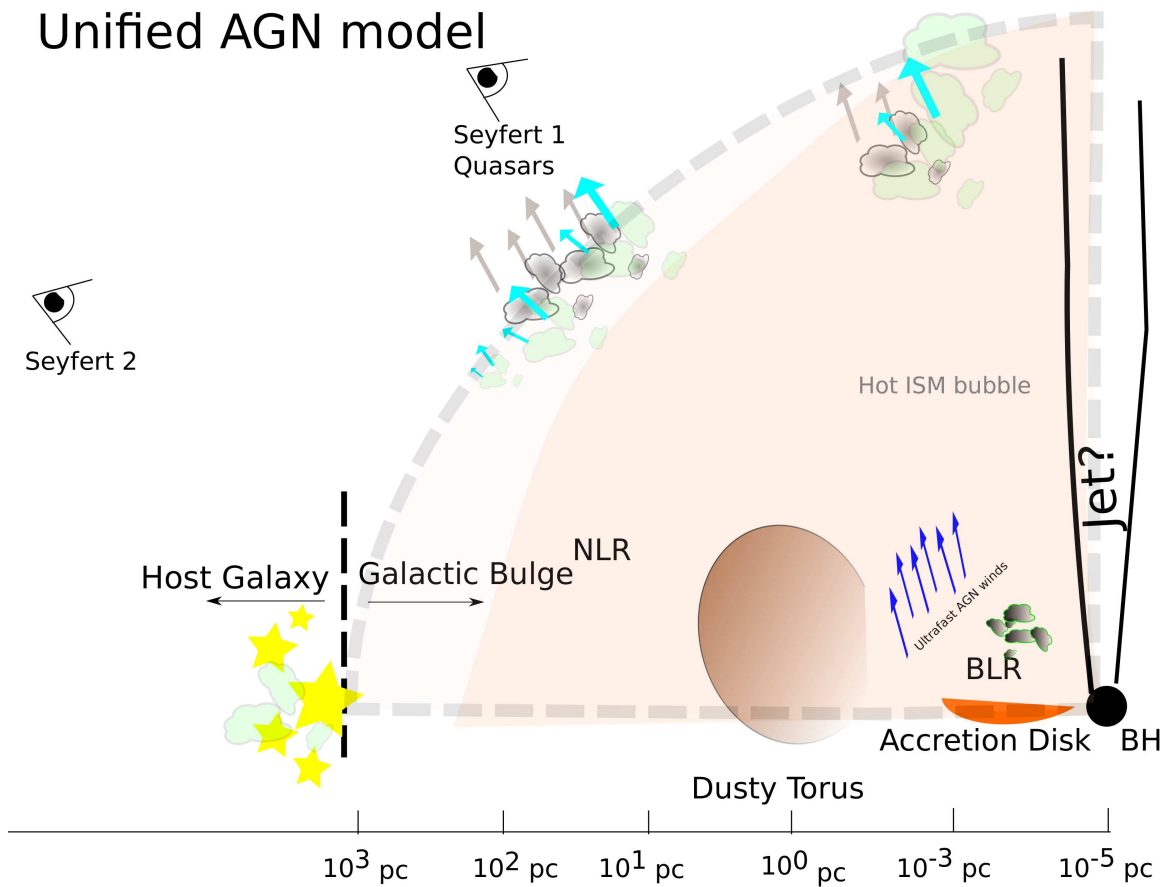
Fig. 1.1 Schematic representation of AGN and the underlying components, giving rise to a large scale outflows of gas. The size of the various components is not in scale. The radial separation, between the multiple components could vary and was put just for reference adapted from Blandford et al. (1990).

Supermassive black holes (SMBHs) have been proposed to play an important role to circumvent this problem. SMBHs are now accepted to be very ubiquitous in galaxies (Magorrian et al. 1998; Ferrarese & Merritt 2000; Gebhardt et al. 2000, e.g.) and able to release tremendous amount of energy when they happen to accrete matter. In such case they are known as Active Galactic Nuclei (AGN). In the standard "Unified" Model for Active Galactic Nuclei (Fig. 1.1) the SMBH is actively accreting material from a surrounding accretion disk. The gravitational potential energy, released as a consequence of the infall of material, is released in the form of radiation, peaking in intensity at ultraviolet (UV) wavelengths. The UV photons given off by the accreation disk are believed to irradiate in first place high velocity clouds of gas in the immediate vicinity of the SMBH, at pc scales. Directly influenced by the gravity of the SMBH such clouds would have to move very fast, thus providing explanation for the broad $H\alpha$ and $H\beta$ emission lines observed in the spectra of bright and

distant Quasars and Seyfert 1 galaxies. The region close to the galactic centre, where such lines would originate is thus labelled as the broad-line region (BLR).

Further outwards at the pc scale, this system is embedded in an optically and possibly geometrically thick dusty torus. Such a structure absorbs the photons, emitted by the acctetion disk, obscuring and blocking the direct view towards the central SMBH and the accretion disk along some lines of sight. Photons escaping this obscuring screen, can still photo-ionise gas further out beyond the BLR, and produce the observed narrow emission lines in the spectra of Seyfert 2 galaxies. The region where such emission lines originate is called the narrow line region (NLR), since it is occupied by clouds of ionised gas that move more slowly and regularly (possibly in a disk configuration) in the galaxy potential thus producing narrower emission lines as observed in Seyfert 2 galaxies. Under these assumptions, what differentiates the two types of Seyfert galaxies is the line of sight of the observer. In Seyfert 1 galaxies the observer has a clear view to the BLR, whereas in Seyfert 2s this view is blocked by the dusty torus. Seyfert AGNs are the most common and powerful kind of active nuclei in the nearby Universe, but the same distinction and explanation for objects showing only narrow nuclear emission or also broad lines applies also to other kind of AGN activity, such as that observed in the Low-Ionisation Nuclear Emission Regions (LINER) of nearby galaxies or the much brighter and distant Quasars.

Two 'modes' of feedback from the SMBHs have been proposed and implemented in simulations, characterised by the accretion rate onto the SMBH itself: radiative ('quasar') mode, when high accretion rate is extant and where the gas is driven mostly by the thermal coupling with the radiation given away in the accretion process and the mechanical ('radio') mode, when the black hole accretion rate is lower and we observe the formation of AGN-driven bubbles (Sijacki et al. 2007) in the hot gas surrounding the galaxy which are carved by radio jets powered by the AGN. Using X-ray and UV spectroscopy, fast winds and outflows originating close to the accretion disk have been observed in luminous Quasars and Seyfert galaxies. These winds are common and considered to be spanning substantial solid angle, if not quasi-spherical in nature. As the wind propagates it would encounter a denser region of the interstellar medium (ISM). Depending on whether the momentum or the energy of the wind is passed onto the ISM, and with what efficiency, the wind could further produce a larger-scale momentum- or energy- driven outflow, sweeping the ISM gas in the host galaxy. Another possible mechanism that might drive a large-scale outflow, is the direct coupling of the radiation, given off by the SMBH to the gas and dust in the centre of the host galaxy. The gas in the ISM need not to be optically thick, however, allowing for the radiation to pass with very little effect (King & Pounds 2015). Powerful jets, arising from the vicinity of the SMBH, could also deposit significant amounts of energy into the ISM so that ambient gas

could be pushed, heated, and shocked by the penetrating jet to produce a large-scale outflow (Davis et al. 2012).

Compelling observational evidence for the existence of large-scale outflows in galaxies with AGN varies with epoch and physical scale, however (Fabian 2012). A specific case of a nearby spatially resolved galaxy, with an outflow on galactic scales, is NGC 1266. In this object an outflow of molecular gas was observed directly through mm-wavelength observations (Alatalo et al. 2011) and indirectly by observing a blue-shifted interstellar absorption, due to Sodium (Davis et al. 2012).

Galaxies, showing particularly strong Sodium spectral features than expected from photospheric lines in stellar population models, hence, are good candidates for testing the presence of AGN-driven outflows hosts. An excess in the optical Sodium spectral complex NaI (Na D) at $\lambda\lambda 5890, 5896$Å has generally successfully been associated to the presence of cold-gas in the interstellar medium, for instance in the disk of our Galaxy (Hobbs 1973; Spitzer 1948), or from gas entrained in a large-scale gaseous outflows in nearby galaxies. Infrared-luminous (Rupke et al. 2002, 2005b; Krug et al. 2010; Heckman et al. 2000; Martin 2005, e. g.), dwarf (Schwartz & Martin 2004) and star-forming galaxies (Sato et al. 2009; Chen et al. 2010), indeed, often display a blue-shifted excess of Na D absorption identified as starburst-driven outflows. In such outflows, driven by the period of intensive star formation,the thermal or/and mechanical energy and momentum, generated by stellar winds and supernovae, is transferred into the surrounding ISM giving rise to kpc-scale outflows with large opening angles. Starburst-driven large-scale outflows display a variety of morphologies, taking different appearance from egg-shaped circum-nuclear structures to having either bipolar double-loop or bi-conical geometry. Large amounts of dust is prevalently found to be entrained in these galactic-scale winds, exhibiting excessively complex spatial distribution. The ISM, being propelled, is truly multi-phased as the outflow of gas has been inferred trough a multitude of tracers, including ionised-gas emission, ultraviolet absorption-lines spectroscopy, and shocked X-ray emitting regions (Veilleux et al. 2005). In the case of infrared-ultra-luminous AGN/star-burst-composite (Rupke et al. 2005b) galaxies it is intrinsically difficult to discern the main driving mechanism (AGN or starburst), but when such distinction was possible it was found that the winds are most likely driven by a compact central star-burst (Sell et al. 2014). Evidence for AGN-driven cold-gas outflows detected through an Na D excess remains more sparse, however (Krug et al. 2010; Lehnert et al. 2011).

In fact, it is important to note that a stronger Na D absorption feature need not always to be due to interstellar absorption by a substantial amount of interstellar matter. Indeed, if intrinsic variations in the stellar-population properties of our galaxies cannot be accounted

for by the stellar population models used to match the spectra, this may also lead to a mismatch in the Na D absorption lines region that could also be mistaken for interstellar absorption. The stellar spectrum of galaxies is most often modelled using a number of so-called Simple Stellar Populations synthesis model (SSPs). These SSPs assume that stars are born at the same time, with the same metallicity and with a given initial distribution of stellar masses, which is also known as the stellar Initial Mass Function or IMF. The evolution of such single-age stellar population is followed by means of theoretical isochrones, which are used to synthesise the overall spectrum of such a stellar population at any given age, using as building blocks either real spectra of nearby stars in the Milky Way or theoretical models of stellar atmospheres (Peletier 2013). Finally, when modelling real galaxy spectra, several SSPs models of different ages and metallicity can be added up to mimic an extended star-formation history or the chemical self-enrichment that typically sees younger stellar populations being also more metal-rich than older ones.

Despite their tremendous success in capturing the main properties of the stellar populations of galaxies, SSPs do not always match in details the strength of many absorption-line features. Also some of the SSP models assume a Solar pattern for the relative abundance of the various elements in stellar atmospheres, which works well when matching the integrated spectra of disk galaxies but often fails to accurately match in massive early-type galaxies the strength of the spectral features due to specific elements such as Magnesium in the case of the Mgb absorption feature at around 5200Å. Indeed, the relative abundance of Magnesium and other alpha-elements is significantly boosted in the stars of these galaxies, compared most often to that of Iron. Such an alpha-over abundance results from the very short star-formation history in early-type galaxies, which is very different from that in typical galactic disks where stars form continuously and which prevented the recycling of material expelled by stars and supernovae that explode only after several hundred Myr.

Similarly, SSPs can also fail to reproduce the observed strength of the Na D stellar feature, even in the absence of interstellar absorption. Most likely, this could be due either to a different shape of the IMF than assumed in the SSP models (typically taken to be as found in the Milky Way), or to an excess in the abundance of Sodium. As regards to the first cause, constraining the shape of the initial mass function (IMF) for a stellar population, given only its integrated spectrum, is intrinsically a difficult task. Indeed, if a substantial amount of the total stellar mass of a galaxy is in the form of low-mass stars, they contribute only as little as one percent towards the total luminosity. In galaxies with 'young' stellar populations (most often found in late-type galaxies) most of the light comes from high mass stars ($\geq 8 M_\odot$), whereas in older stellar populations these stars would be in their final evolutionary stages and would no longer account for such a great fraction of the luminosity

budget. In older stellar population (found in most early-type galaxies) the integrated light is dominated by K and M giants, but the bulk of the stellar mass is in the form of cool K and M dwarf stars. Even though such dwarfs and giants are of the same spectral type, and therefore share similar effective temperature, the higher surface gravity of the dwarfs enhances the strength of certain absorption lines, including the Na D lines, arising in their photospheres (Conroy & van Dokkum 2012a). A number of recent studies have indicated that in massive early-type galaxies the IMF could show a steepening at its low-mass end (van Dokkum 2008; Conroy & van Dokkum 2012a; Spiniello et al. 2012; Conroy & van Dokkum 2012b), alluding that in such galaxies the observed enhancement in the strength of the Na D feature as well as in our sample could also be due to a greater number of low-mass dwarf stars.

Concerning the second possible cause for an intrinsic enhancement of the photospheric Na D feature beyond what is predicted by standard SSP models, that is, an intrinsic over abundance of Sodium, recent work also points toward such an enhancement occurring towards the central regions of early-type galaxies or galactic bulges (Zieleniewski et al. 2015; McConnell et al. 2016). In this case, such an over-abundance could stem from a combination of a very short star-formation history and super-Solar metallicity in these objects. Indeed, the yields of Sodium from Supernovae Type II, which are triggered by the explosion of very massive stars, do increase as a function of metallicity (Kobayashi et al. 2006), so that stars may have had a chance to enrich themselves in Sodium during the main star-formation episode experienced by early-type galaxies.

In this work we investigate the kinematics of the Na D excess in a sample of Sodium excess galaxies (Jeong et al. 2013) and correlate it to some derived galaxy properties (i.e. morphology, reddening by dust, stellar velocity dispersion) in order to understand, if its origins relate to stellar populations effects or to the presence of interstellar absorption. In this last case we will then check whether the Na D kinematics indicate a substantial fraction of outflowing and escaping gas, and further check if this could relate to the presence of an AGN.

Chapter 2

Origin and Profile of the Na D Absorption

2.1 The Optical Sodium Doublet

In order to obtain accurate understanding of the interaction between radiation and matter, modern spectroscopy utilises atomic physics. The origin and behaviour of observed spectral features is governed by the physical processes that occur at microscopic scales in the system of interest. The Sodium absorption doublet in the optical (Na D) originates from Na in neutral state and since Sodium has a low ionisation potential (5.13908 eV) the detection of Na D absorption traces cold gas even at modest optical depths in the presence of an illuminating source. The Na D absorption feature arises from the electron transitioning from either the $P^2_{1/2}$ or $P^2_{3/2}$ to the $S^2_{1/2}$ state, due to the spin-orbital coupling of the orbital angular momentum and the spin of the electron. An important quantity, derived using detailed quantum mechanical calculations, widely applied to spectroscopic analysis is the oscillator strength (f), describing an atom as a classical oscillator (dipole) of such strength in total absorption to electromagnetic radiation (Jefferies 1968). This is also called the *absorption f-value* and is a dimensionless quantity, related to the atomic absorption cross section at a given frequency of radiation s_ν. It defines the effectiveness of a transition in terms of an equivalent number of classically behaving electrons, each with a classical cross section, assuming the a radius of the cross section of $e/m_e c^2$ (where e is the charge of the electron, m_e is the electron mass, and c is the speed of light) in absorbing radiation of specific frequency. The degeneracy of the transition level $g = 2J + 1$ is the number of possible configurations of the total angular momentum that have the same energy. For the transition giving rise to the 'red' line in the doublet $J = 1/2$, therefore $g_{red} = 2$. Likewise $g_{blue} = 4$, since for the

'blue' line at 5895.92Å - $J = 3/2$. From Arav et al. (1999) with the values for Sodium of Morton (2003) the ratios of the optical depth as measured by the centroid of the doublet line for both transitions (the blue-er and red-er line in the doublet) arising from the same level (neutral) Sodium the intrinsic optical depths ratio of the two lines is:

$$r_{\tau} = \frac{\lambda_{red} f_{red} g_{red}}{\lambda_{blue} f_{blue} g_{blue}} \approx 1/2. \tag{2.1}$$

2.2   The Physics of Emission and Absorption

Following Spitzer (1978) the change of the specific intensity I_{ν} of light as a result of an interaction with matter for photons travelling in straight lines along a distance dl of a light ray, is given by the 'equation of transfer':

$$\frac{dI_{\nu}}{dl} = -\kappa_{\nu} I_{\nu} + j_{\nu}, \tag{2.2}$$

where κ_{ν} and j_{ν} are the absorption and emission coefficients, taken such that energy emitted or absorbed by a given element of volume dV in the frequency interval $d\nu$, within a solid angle $d\omega$ and time dt would be described as $j_{\nu} dV d\nu d\omega dt$ and $\kappa_{\nu} I_{\nu} dV d\nu d\omega$ respectively.

Defining $d\tau_{\nu} = -\kappa_{\nu} dl$ or the optical depth (thickness) and substituting in equation 2.2:

$$\frac{dI_{\nu}}{d\tau_{\nu}} = I_{\nu} - \frac{j_{\nu}}{\kappa_{\nu}} \tag{2.3}$$

The solution of this ordinary differential equation can be obtained by integrating from 0 to $\tau_{\nu o}$:

$$I_{\nu} = I_{\nu o} e^{-\tau_{\nu o}} + \int_{0}^{\tau_{\nu o}} \frac{j_{\nu}}{\kappa_{\nu}} e^{-\tau_{\nu}} d\tau_{\nu}, \tag{2.4}$$

where $I_{\nu o}$ is the intensity of the source at the far side of the emitter and/or absorber and $\tau_{\nu o}$ is the total optical thickness. The quantity j_{ν}/κ_{ν} is usually referred to as the *source function* (S_{ν}). In the general case, both emission and absorption of photons would take place as the radiation passes through the matter slab, changing the specific intensity of the light. Most generally, given the specific physical conditions, applicable to a particular case, a source function is constructed, such that it reflects the relevant physical processes giving rise to the emission of radiation and reflecting the variety of mechanisms that lead to the absorption of photons. For the purpose of our investigation we are concerned only with the specific case of a homogeneous (κ_{ν} independent of l) absorber of matter. Therefore, we

consider only absorption and hence neglect the effects of scattering and assume no emission of radiation from the medium ($j_\nu = 0$). For this specific case the solution would be reduced to:

$$I_\nu = I_{\nu o}e^{-\tau_{\nu o}} \tag{2.5}$$

The value for the intensity of the radiation emitted at the far side of the line-of-sight is $I_{\nu o}$. The optical depth is taken such that $\tau_{\nu o}$ is the value of the optical depth at the far side of the line-of-sight through the absorber and at the observer $\tau_\nu = 0$.

The absorption coefficient κ_ν (volume opacity) in units of inverse length can be parametrised in terms of the *absorption cross section per particle* (s_ν) and the density of the particles, undergoing absorption (n):

$$\kappa_\nu = ns_\nu, \tag{2.6}$$

It is most often convenient to express the dependence of κ_ν and respectively τ_ν on ν in terms of the so-called *line shape function* $\phi(\Delta\nu)$. This function is chosen to be normalised to unity $\int_{-\infty}^{\infty} \phi(\Delta\nu)d\nu = 1$. It has dimensions of 1 over frequency (time) and reflects the distribution of frequencies of the absorbers, each having cross section per particle (s_ν). This absorption cross section per particle is directly proportional to the absorption coefficient κ_ν and its frequency-integrated equivalent is labelled the *integrated absorption cross section* (s) and is equivalent to taking the integral $s = \int s_\nu d\nu$ over the frequency range. The line shape function can take different forms in accordance to the conditions the absorber is subjected to (e.g. the atoms can for example undergo collisions) and is also dependent on the intrinsic line width (natural broadening). The electron transitions giving rise to the formation of the spectral lines do not correspond only to a certain energy difference in the energy of the electron, absorbing or emitting the photons. Instead, the energy of the electron is in reality spread around the most probable energy, so that the absorbed photons are not of just a precise frequency or wavelength, but absorption lines spread over a small wavelength or frequency interval. In the most simple case the width of the line, arising from such effects, is small and can be effectively ignored.

For simplicity we adopt the case of an absorbing gas in a thermodynamic equilibrium and consider the line broadening only due to the motion of the constituent atoms. The atoms in the gas would follow a Maxwellian velocity distribution and the shift in frequency due to the motion of the particles along the line of sight would be given by the Doppler formula describing the shift of frequency $\Delta\nu$ or wavelength $\Delta\lambda$ for an atom moving with at a certain velocity V:

$$\frac{V}{c} = \frac{\Delta\lambda}{\lambda_c} = \frac{\Delta\nu}{\nu_c}, \tag{2.7}$$

where V is the velocity of the particle (atom) absorbing, $\Delta\nu$ is the difference between the absorption frequency ν and the frequency at the line centre ν_c, and c is the speed of light.

Using the Doppler formula and extrapolating to a distribution of atoms with Maxwellian velocities the line shape function for a single line-of-sight $\phi(\Delta\nu)$ would be:

$$\phi_l(\Delta\nu) = \frac{c}{\sqrt{\pi}b_D\nu_c}e^{-(V/b_D)^2}, \tag{2.8}$$

The quantity b_D is called the *Doppler parameter* and it denotes the dispersion in the speeds of the absorbers in the radial direction $\sigma = b_D/\sqrt{2}$. In the case of pure thermal broadening the Doppler parameter for the gas is a simple function of the temperature and the atomic weight of the underlying particles. This line profile function would be generally true for the line-of-sight, if no general net preferred bulk macroscopic difference and/or motion in the gas is present (isotropic gas). Therefore in our simple case taking the integral of $d\tau_\nu = -\kappa_\nu dl$ over the line-of-sight would be equal to:

$$\tau_{\nu o} = Ns\phi_l(\Delta\nu), \tag{2.9}$$

with N defined as the *column density* of the absorbing atoms $N = \int ndl$ in units of inverse area.

From eq. 2.10 substituting for V the expression from eq. 2.7 in eq. 2.8 in terms of $\Delta\lambda$ and taking $\lambda_c = c/\nu_c$ we obtain an expression for $\tau_{\lambda o}$:

$$\tau_{\lambda o} = \tau_0 e^{-(\frac{\Delta\lambda}{\lambda_c b_D/c})^2}, \tag{2.10}$$

where $\tau_0 = \frac{Ns\lambda_c}{\sqrt{\pi}b_D}$ is usually referred to as the *central optical depth* or the optical depth at the centre of the line. Substituting back in eq. 2.5 we can obtain the expression for the intensity of the source after the absorber:

$$I_\lambda = I_{\lambda o}exp(-\tau_0 e^{-(\frac{\Delta\lambda}{\lambda_c b_D/c})^2}) \tag{2.11}$$

2.3 The Line Profile Parametrisation

The two Sodium doublet lines in the optical spectral region have a separation of $\approx 6\text{Å}$, which corresponds to a velocity shift of $\approx 300\text{km s}^{-1}$. This is well within the reach of modern spectrographs, enabling us to try and de-blend the Na D lines and investigate their
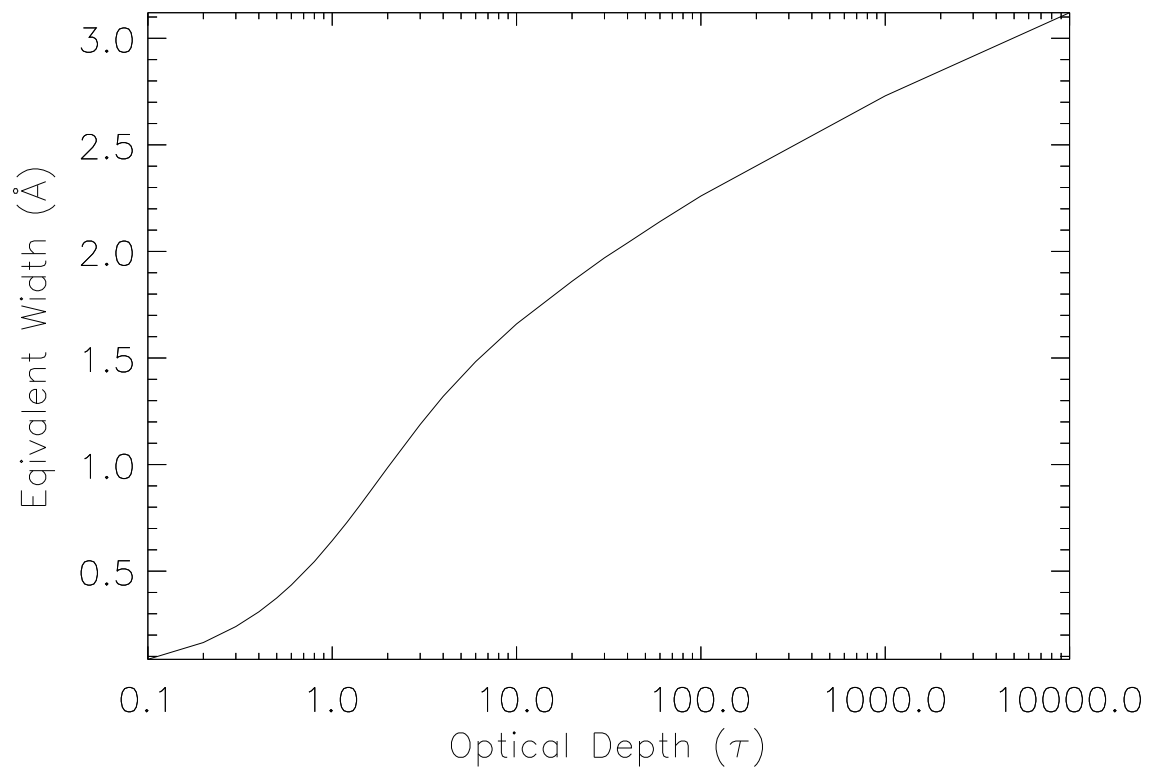
Fig. 2.1 The so-called curve-of-growth. Tabulated from Spitzer (1968).

spectral profiles. In case of a large velocity broadening or in the presence of a complex spectral shape for the light source, such as the spectrum of a galaxy, inferring directly the line profile may not be that straightforward. This will be the case of our observations, for instance, where instead we will assume a given shape for the absorption profile of the Na D lines.

When resolving the lines is possible, the profile of absorption lines is most often parametrised in terms of simple functional forms, such as Gaussian, Lorentzian, and Voigt profile. These functional forms for the spectral profiles can easily be used under certain assumptions.

The Lorentzian profile describes well the intrinsic profile for the case of natural broadening. The Lorentzian profile also describes well the intrinsic profile when the constituents of an absorber do also undergo collisions and get scattered. If the particles interact and excite one another at a time scale compatible to the amount of time in which the emission and/or absorption occurs, the effects of these interactions would be significant and the line profile will show pronounced "wings" on either side of the main intensity peak around the central frequency or wavelength of the line. Under such conditions the line is said to be dominated by collisional (or pressure) broadening. The Gaussian profile for a spectral line is generally used when the broadening of a line is considered to be dominated by either the intrinsic thermal motion of the absorbing particles and/or ordered motion (i.e. rotation). Finally, a spectral line is defined in terms of the Voigt profile when the underlying principles giving rise to both the Lorentzian and Gaussian profiles are important. The Voigt profile is effectively the convolution of these two previously described functional forms.

In the cases when the spectral resolution does not allow to resolve the true line profile, most often a substitute measurement is adopted. It is most convenient in such cases to define the equivalent width (EW) of a line in terms of the intensity and the wavelength of the radiation measured as:

$$W_\lambda = \int_0^\infty \frac{I_\lambda^C - I_\lambda}{I_\lambda^C} d\lambda, \tag{2.12}$$

where the intensity of the so-called continuum is given by I_λ^C and represents the intensity at the far side of the absorber, where absorption is absent, and the actual intensity trough the line profile is expressed by I_λ.

Even when only measurement of the equivalent width of a line is accessible, it is still possible to gain some information for the physical conditions and properties of an absorber. The EW of a line is a measure of the strength of the line that is somewhat independent of the line profile. On the other hand, the depth of a spectral line depends on the number of absorbing particles, the nature of these particles, and it varies in accordance to the shape of

the line profile function (e.g. Gaussian, Lorentzian ot Voigt). The relation between the EW of a line and the column density (N) of the absorbers, or an equivalent quantity, such as the central optical depth, is called the $curve-of-growth$. Figure 2.1 shows the log-log relation between the optical depth as evaluated at the line centre and the equivalent width for an absorption spectral line. The optical depth, as evaluated at the line centre, is dependent both on the column depth and the broadening mechanism of the line. Starting with a small amount of absorbers the line is in the optically thin regime, where the number of absorbers will be directly proportional to the EW of the line, almost regardless of the line profile shape. In this regime the curve of growth is termed to be on its 'linear' section, where lines dominated by Doppler broadening show a Gaussian profile. As more and more absorbers are added the line continues to increase in strength, until the maximum amount of flux is removed at the line centre. The line is no longer optically thin, but optically thick, and is said to be 'saturated'. In this specific regime just the EW of the line is no longer a good proxy for the number of absorbers, the line is now on the 'flat' section of the curve. From the previous section, looking purely at the case of Doppler broadening, the optical depth at the line centre is inversely proportional to the Doppler parameter. Therefore, broader lines would saturate more slowly than narrower ones. If even more absorbing material is added, the line continues to saturate and at a given threshold collision between the particles of the absorber start to produce stronger 'wings' and the spectral profile is best described by a Voigt function. The EW is again independent of the Doppler parameter. Under such considerations, if the absorbing gas is optically thick, just the EW width of the lines especially in a doublet can no longer be reliably utilised to deduce the amount of absorbers present. Only if the lines are optically thin and not heavily saturated would the Maxwellian intrinsic velocity distribution translate to a Gaussian in intensity under in the line-of-sight (Spitzer 1978).

The problem is even more complicated in the case of blended absorption doublets such as Na D. Using the intrinsic oscillator strengths, the optical depth at the line centre for the 'blue' line (5889Å) in the doublet is twice the one at the centre of the 'red' line. Yet, as the lines saturate, not only could the shape of the lines deviate from a simple Gaussian, but this ratio for the apparent optical depths (amplitudes of the lines) at the line centres also changes from 1:2 to 1:1. In such a scenario, fitting Gaussian profiles to the individual lines of the doublet might lead to unphysical ratios of their amplitudes. Hence, if the two lines are blended, it becomes more difficult to retrieve the individual EWs of the lines and use the so-called 'doublet ratio method' (Strömgren 1948) to deduce the apparent gas column density, as it was done in classic studies for the abundance and distribution of the interstellar medium in the direction of single stars in the Milky Way (Spitzer & Lautman 1956; Nachman & Hobbs 1973, e.g.).

In the case of external galaxies, the situation is even further complicated by the fact that our observations capture a multitude of overlapping clouds absorbing light from an extended stellar source. In this case, even if the absorption lines from each single cloud are not saturated with an intrinsic Maxwellian distribution for the particles in each cloud, the resulting line profile will generally depend on the overall line-of-sight velocity distribution (LOSVD) of the clouds and on the geometry of the system (for instance, to what extent they are obstructing the extended source). Jenkins (1986) demonstrated, however, that the effects of the LOSVD distribution of the clouds on the line profile are not of particularly great importance in most simplistic cases of power-law and bi-variate Gaussian distribution for the absorbing clouds, pointing out that the line profile could therefore still be Gaussian provided that the cloud LOSVD is not too irregular. In some instances, there are reasons to consider a covering fraction and an optical depth of the clouds that depend on the velocity and geometry of such absorbers. In this case, an advanced analysis is needed to account for the line profile, as shown by Arav et al. (1999) for Quasars and by Fujita et al. (2009) for outflowing gas in intensely starbursting galaxies.

In this work we will not be concerned with such extreme cases as Quasars or Ultra-Luminous Infrared Galaxies (Rupke et al. 2005b), but with rather regular galaxies where the Na D absorption profile does not appear exceedingly complicated. Drawing from previous work on nearby galaxies with an excess of Na D absorption, based on data with a similar spectral resolution to that of our spectra, we will work under the simplest assumption of Maxwellian velocity distribution for the absorbing clouds along the line-of-sight and that the covering fraction of such clouds is itself independent of velocity. Furthermore, we will consider one single set of absorbing clouds in our sample galaxies, although more gaseous components, with different geometries and kinematics, may be present.

Chapter 3

Sample and Modelling

To investigate the nature of Sodium excess objects and look for evidence of AGN- induced outflows in the local Universe, in this thesis we adopted the sample of Jeong et al. (2013). This group performed the first systematic search for galaxies with an enhanced Na D absorption, using spectra from the Sloan Digital Sky Survey (SDSS) data release 7 (DR7) (Abazajian et al. 2009) by inspecting the residuals of the spectral fitting, provided by the database of Oh et al. (2011, OSSY). The OSSY fits are based on the the Cappellari & Emsellem (2004) Penalized Pixel Fitting Method (pPXF) and the Gas AND Absorption Line Fitting (GANDALF) code of Sarzi et al. (2006), which combine stellar and Gaussian templates to provide optimal fit to a galaxy stellar continuum and emission-line spectrum. For the purpose of their investigation Jeong et al. defined an f_{NaD} index:

$$f_{NaD} = \frac{NaD(Observed) - NaD(Model)}{NaD(Model)},$$

where Na D(Observed) is the observed Na D absorption-line strength and Na D(Model) is the expected photospheric absorption strength, provided by the best-fitting model for the stellar continuum. In OSSY this was achieved with both the Bruzual & Charlot (2003) stellar population models and by means of the semi-empirical stellar templates from the MILES stellar library of Müller-Sánchez et al. (2011). The latter were obtained by matching the spectra of emission-free galaxies and were used to improve the deviations from the models due to template mismatch, in particular those due to an enhanced abundance of α elements (e.g. Mgb absorption-line feature). Since in this work we are also interested in identifying the impact of an enhanced Na abundance in the observed Na D excess of our galaxies, we decided to restrict our stellar continuum fit only to the stellar population model templates of Bruzual & Charlot (2003), which adopt a Solar Na abundance. During these new pPXF and GANDALF fits we also obtained new emission-line and dust-reddening measurements,
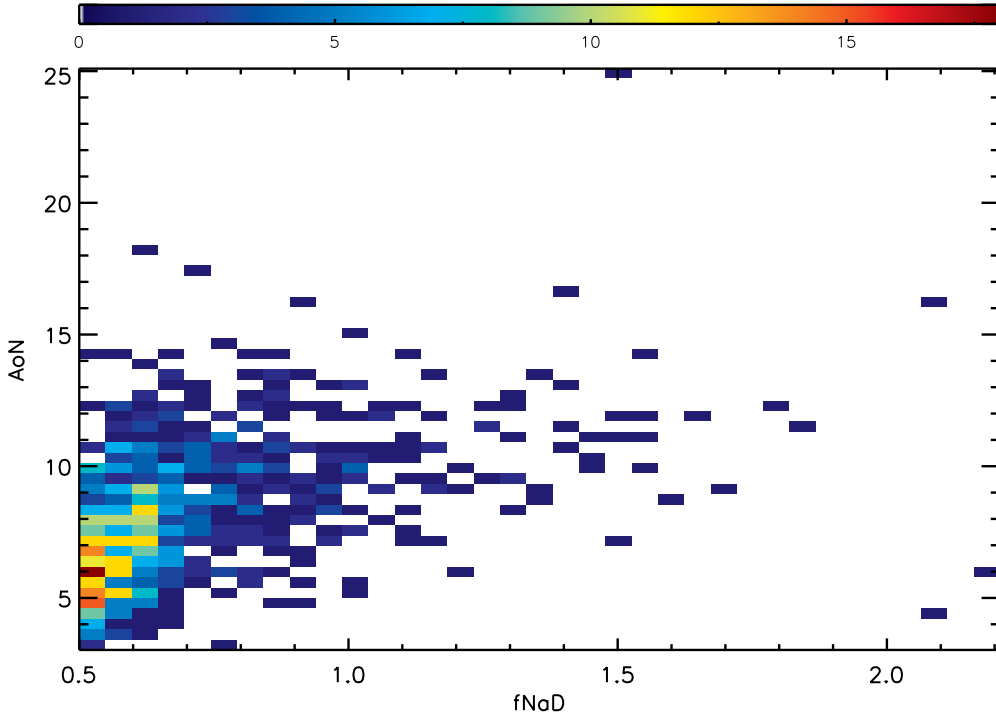
Fig. 3.1 Density plot with f_{NaD} and A/N for the additional Na D kinematic component.

but since these are consistent with the OSSY catalogue, we decided to stick to the latter measurements.

Jeong et al. adapted a threshold of $f_{NaD} \geq 0.5$ to define objects, showing excess in Na D (NEOs). According to this classification a $f_{NaD} = 0.5$ index value would correspond to observed absorption strength one and a half times stronger than what is predicted by the OSSY stellar-continuum model. A first result of our dedicated fitting of the Na D feature revealed that the signal-to-noise for the Na D excess - or better the amplitude-over-noise (AoN, A/N) of the fitted Na D excess profile is consistently higher than 3 (the requirement for detection of emission lines of Sarzi et al. 2006, which should apply also to the Na D profile - see §3.3 [1]), even for objects at the Na D detection threshold of Jeong et al. (Fig. 3.1). When defining their Na D excess detection threshold, Jeong et al. further imposed a redshift cut $(0.00 \leq z \leq 0.08)$ and an absolute r-band magnitude limit of -20.5 magnitudes, which allowed for a robust morphological classification for the NEOs and for good quality spectra. The condition was further ensured by selecting only objects with a minimum spectra signal-to-noise (S/N) of 20 and for which the OSSY fits where sufficiently good (i.e with a residual-to-statistical noise ratio $rN/sN \geq 1.5$).

---

[1]The AoN is evaluated by taking the troughs profile amplitude for our model and by comparing it to the standard deviation of the residual.

All NEOs were also visually classified by Jeong et al. excluding strongly interacting objects and retaining only four classes. These were: (1) ordinary early-type galaxies (oETG), (2) peculiar early-type galaxies (pETG), (3) ordinary late-type galaxies (oLTG), and (4) peculiar late-type galaxies (pLTG). The ones classified as peculiar show some asymmetric features (dust lanes/patches, shells or tails). Furthermore, all of the objects with detected ionised-gas emission in the sample were classified into: (1) star-forming (SF), (2) Composite (Co), (3) LINER (LI), (4) Seyfert (Se), using the 'Baldwin, Phillips & Terlevich' (BPT) diagram Baldwin et al. (1981) adapting the dividing lines of Kauffmann et al. (2003) , Schawinski et al. (2007), and Kewley et al. (2001) to separate the various emission- line objects. Finally, objects with no or only weak emission were grouped in the (5) no-emission (NE) category.

The pixel size of SDSS spectrum is $\simeq 69 \mathrm{km\,s^{-1}}$ and thus the optical Sodium D feature is well resolved. By obtaining the kinematics we aim to investigate the correlations between the Sodium excess, present in our sample, and the properties of the host galaxies.

3.1   Modelling the Sodium Na D Profile

To model the profile of the absorption excess in our sample galaxies we decided to follow the approach of Sato et al. (2009). The line profile parametrisation of Sato et al. (2009) essentially assumes a Maxwellian distribution for the velocity of the absorbing gas clouds and that their covering fraction is independent of the velocity. In this framework we implicitly consider single component of Na D absorbers, although it can be argued that in some cases at least two components could be present. For instance, in galaxies outflowing gas could co-exist with a relaxed component in the disk. Similarly, a second absorbing component at rest with the galaxy could be used to mimic the presence of an enhanced Na photospheric absorption, in addition to a real interstellar absorbing component. In this study we decided to adopt only one kinematic component to model the Na D excess profile, since for the vast majority of our sample galaxies this approach already produced a good fit. Furthermore, while both our results (see §4) and the visual inspection of the residuals for some of our worst fits could suggest the presence of a second Na D component, preliminary experiments with an additional kinematic component did not yield a statistically significant improvement to the quality of the fit. In fact, we found that our main minimisation workhorse, the MP-FIT procedure (see below), was not particularly stable when including the extra parameters corresponding to such an additional Na D component. Adopting a Bayesian analysis based on Monte Carlo Markov chains (MCMC) would be best suited for this purpose, as this approach indeed is also more robust in the case of a single component (see §4.5).

Now, following Sato et al. (2009) and their assumptions the absorption line profile for the Na D doublet can be expressed as:

$$I(\lambda) = 1 - C_f[1 - \exp[-2\tau_0 e^{[-(\lambda-\lambda_{blue})^2/(\lambda_{blue}b_D/c)^2)]}$$
$$- \tau_0 e^{[-(\lambda-\lambda_{red})^2/(\lambda_{red}b_D/c)^2)]}]],$$

where in the previous expression τ_0 is the line centre optical depth, C_f is the so-called covering fraction, b_D is the Doppler parameter (corresponding to $\sqrt{2}$ times the clouds velocity dispersion σ), and $\lambda_{red} = 5889.9510$Å and $\lambda_{blue} = 5895.9242$Å are the rest-frame central wavelengths for the red and blue lines of the Sodium doublet. Figure 3.2 shows this profile parametrisation as a function of τ_0 for a Doppler parameter of $100\,\mathrm{km\,s^{-1}}$ and for covering factors of C_f of 0.25 and 0.75. For clarity the Na D profile for C_f of 0.75 is redshifted by $1000\,\mathrm{km\,s^{-1}}$. As expected for an intrinsic Maxwellian distribution the profile of each individual Na line remains Gaussian in the optically thin regime, until saturation enters in play at high column densities. Figure 3.2 also shows how by increasing either C_f ot τ_0 it is possible to obtain similarly strong absorption line profiles, indeed reflecting a strong correlation between these two parameters. As a consequence it is very difficult to break the degeneracy between C_f ot τ_0 and estimate them separately. Note also that in this model, the internal motions of the particles in single gas clouds can be effectively ignored, since this would contribute to a line-broadening of just a few kilometres per second that is much smaller than the line-of-sight velocity distribution of all the absorbing gas clouds.

The Sato et al. parametrization for the absorption profile is matched to the data only after normalizing the observed spectra by our best model for the background stellar continuum, although the absorption profile could be adjusted while fitting directly to the data the product of our best-fitting stellar continuum (and emission when present) and the Na D absorption profile. Working on continuum-normalized spectra is the most common practice, however, due to historic reasons and earlier difficulties in dealing with data of varying spectral resolution and a poor flux calibration. Such problems are indeed circumvented by modelling the stellar continuum using a suitable set of stellar templates (such as G and K giants) observed with same instrument.

As a preliminary step to performing our analysis of the Na D excess profile, we restricted ourselves to the 25 pixels around the Na D position of the stellar Na D absorption feature and divided the observed spectrum by the best-fitting GANDALF model, which includes the best model for the stellar spectrum and for the HeI 5875.60 ionised-gas emission. Using an in-house IDL code we then proceeded to fit any putative Na D excess profile with the model of Sato et al., which gives an estimate for the best-fitting value for τ_0, C_f, b_D, and the central wavelength position of the Na lines, expressed as a velocity shift using $\lambda_{blue} =$
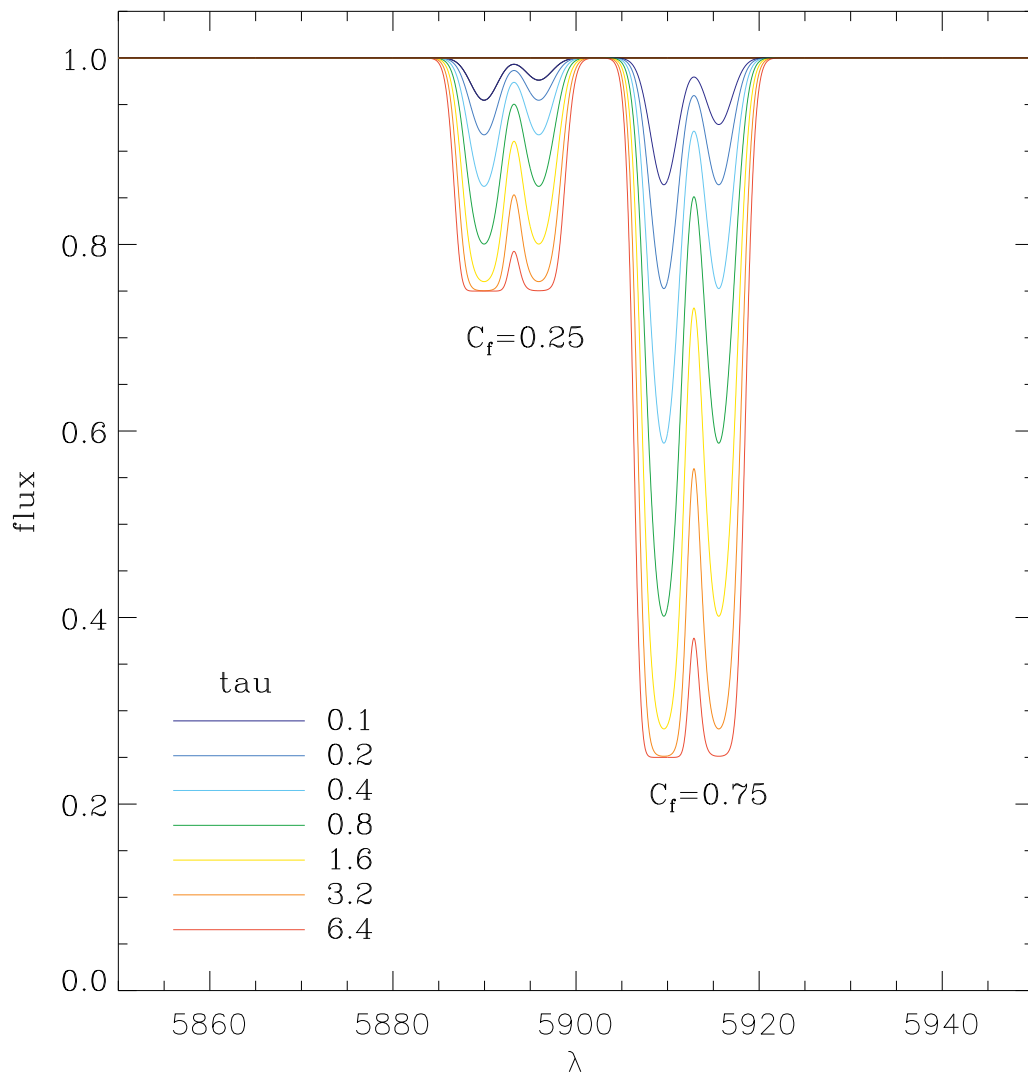
Fig. 3.2 The change in spectral profile shape for the parametrisation of Sato et al. for different τ, while keeping a constant covering fraction C_f.
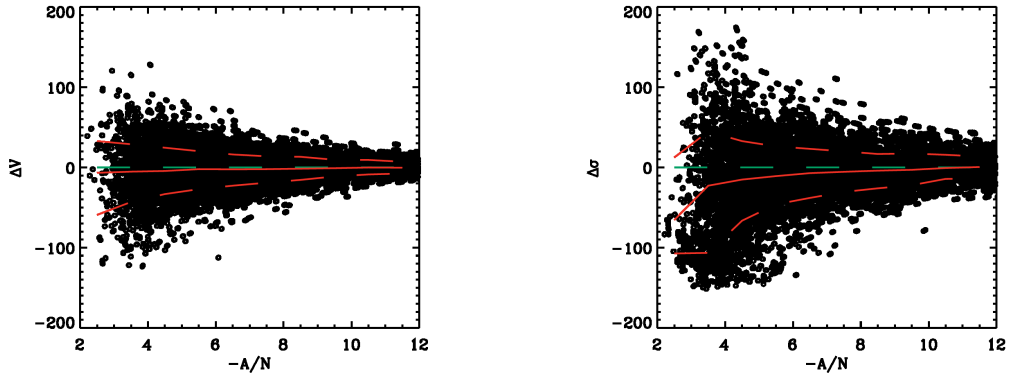
Fig. 3.3 The retrieved deviations from the input kinematics for the case of our simulations at different noise levels. The solid red line gives the median. The dashed red lines are the 16th and 84th percentile of the distribution of the difference. The green line is tracing where the difference is zero. Our fitting procedure is unbiased in velocity up to -A/N of approximately 3 and in regards to velocity dispersion at -A/N of around 4.

$(1 + v_{NaD}/c)\lambda_{blue}$ and $\lambda_{red} = (1 + v_{NaD}/c)\lambda_{red}$. To perform the model fit we use the the Levenberg-Marquardt non-linear least squares curve fitting MPFIT (Markwardt 2009) algorithm, while constraining the parameters to fit within reasonable physical limits: $0 \leq \tau_0 \leq 1000$, $0 \leq C_f \leq 1$, $-700 \leq v_{NaD} \leq 700$, and $40 \leq b_D \leq 700$.

3.2   Quality of the Na D Fit

Before interpreting the results of our Na D profile fitting, we need to ensure that our models provide a good fit to the spectral region. Figure 3.4 shows the distribution for the reduced χ^2 statistic as proxy for the quality of a given model fit to the data, for our fits. On the basis of such reduced χ^2 statistic we decided to exclude all fits with $\chi^2_{red} > 1.5$, corresponding to 96.56% (p-value of 0.0344001) significance level that our model fits the spectrum well. In addition, we also restricted ourselves to objects where we in fact detect an Na D excess absorption profile, by requiring that the profile peak amplitude is at least three times the noise level in the model residuals (i.e. $-A/N > 3$). We adopt such a threshold following not only the results of Sarzi et al. (2006), based on simulations for emission lines, but also on further simulations with the adopted absorption spectral line profile parametrisation. For this, starting from the spectrum of a real galaxy and the best fit for its stellar continuum and nebular emission, we constructed 200949 model spectra with increasing -A/N from 2.21 to
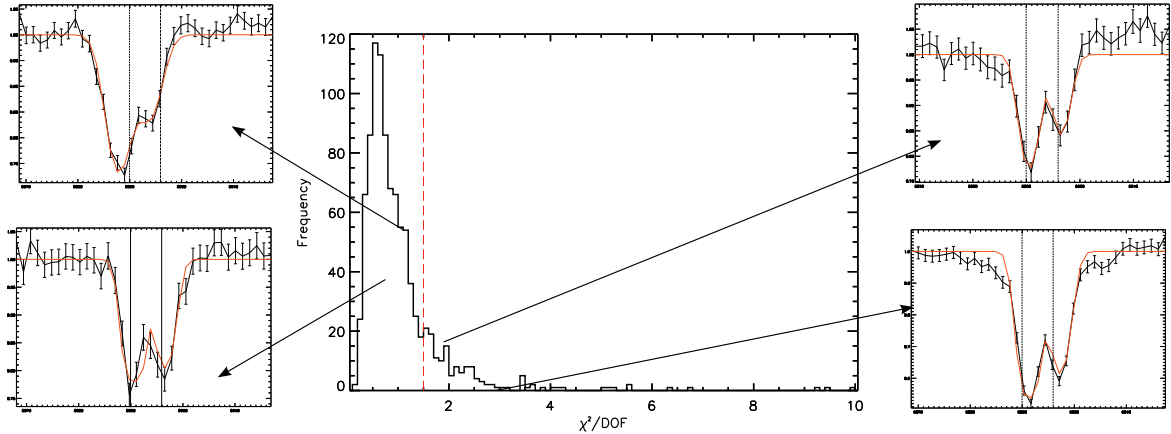
Fig. 3.4 The reduced chi-square distribution for the fit in the Na D region. The arrows point at an example fit, drawn from the specific bin.

Table 3.1 The sample after the 1.5 reduced Chi squared cut.

Type	Excluded	Total	% excluded	Good fit
Star-forming	42	191	22	149
Composite	43	169	25	126
Seyfert	6	25	24	19
LINER	18	85	21	67
No-emission	86	494	17	408

21.22, and with an Na D absorption profile blue-shifted by $200 \mathrm{km\,s^{-1}}$ and with a width of $200 \mathrm{km\,s^{-1}}$ which is representative of those cases where Na D outflow is deemed likely (e.g. Fig 4.1). We then applied our fitting routine to these artificial spectra where, as a result of their decreasing quality, the Na D profile is progressively embedded in the residual noise. Fig. 3.3 shows the deviation from the input values of the retrieved velocity and velocity dispersion of the fitted Na D profile, as a function of the measured A/N. As expected the retrieved values deviate progressively more and more as the A/N drops toward zero. Most important, however, it is clear that for a $-A/N < 2$ and < 4 the retrieved velocity and velocity dispersion become biased. Since we are interested chiefly in the retrieved Na D velocity, we adopt an A/N threshold of three for recovering the Na D profile, consistent to the $A/N > 3$ indicated by Sarzi et al. (2006) in the case of emission lines. This leaves us with 769 galaxies out of our initial sample of 963 objects or 79.7% of the total. Table 3.1 summarises our sample after such fitting-quality and detection cuts.

Inspecting the residuals of our formally bad fits we generally found that these were due to one of the following reasons:

1. MPFIT did not converge to an optimal solution.

2. The He I emission line is particularly strong and not perfectly modelled.

3. The Na D spectral feature had a complex profile.

4. Stellar continuum could not be matched to a small degree.

5. Sky lines were present in the Na D region.

where the most common cause was the small mismatch in stellar continuum or in a very small number of cases the presence of a more complicated line profile. In the latter case, however, we never observed the kind of complications - such as a tail towards bluer wavelength - expected in the case of outflowing gas. Instead, as fig. 3.4 shows, we most often find that the profile would have been best fitted by including a somewhat broader, but weaker component. As it will be discussed later, such an additional component may also reflect template mismatch.

3.3   Some Limitations of Our Model Optimisation

The Levenberg-Marquardt MPFIT algorithm is a fast and robust way to optimise and infer parameters, but unfortunately it might not necessarily retrieve the global minimum in the case of a multivariate parameter space, thus failing to converge around the correct parameter values. A further problem exists when the probability distribution for a parameter cannot be well approximated as a Gaussian or there is some degeneracy between parameters. In such cases, the routine might not lead to correct error estimation, since the error estimation procedure is based on the assumption that near the best parameters the χ^2 distribution can be approximated by a quadratic form, which in turn corresponds to a Gaussian probability function.

To better understand the behaviour of our model around the data depending on the quality of the spectrum and the spectral profile shape, and to look for correlation between parameters, for a subsample of our objects, we proceeded to optimise our modelling procedure by using the Affine Invariant Markov Chain Monte Carlo (MCMC) Ensemble sampler (emcee) of Foreman-Mackey et al. (2013). We used uniform prior with the same boundaries as for MPFIT and ran 20 walkers with 10^5 steps for each walker, starting with a burn-in phase of 50000 steps. Figures 3.5 and 3.6 show - perhaps not surprisingly - a similar behaviour to that in Sato et al. (2009), and in particular that the posterior distributions for τ_0 and C_f can be rather complex and indicative of a strong correlation between these two parameters as

Fig. 3.5 Left: Example of well- constrained parameters for a Seyfert galaxy, where the distributions of the parameters are well approximated by means of Gaussians, yielding a parameter estimation close to the one that would be obtained by MPFIT. Right: The blue line is the model as retrieved by MPFIT. Red line is model for the estimated from MCMC parameters.

suggested also by Fig. 3.2. On the other hand, the posterior distributions for V_{NaD} and b_D were well approximated by a Gaussian in most of the cases, providing reassurance as these are the only two parameters of interest in this work. Nonetheless, Fig. 3.6 shows some instances of the MPFIT fit converging to v_{NaD} and b_D values that are somewhat different from the best values returned by the MCMC method, although generally within the uncertainties of the latter. Still, to firm up our results concerning Seyfert galaxies (§4.5) we will double check our MPFIT-based results with our MCMC procedure.
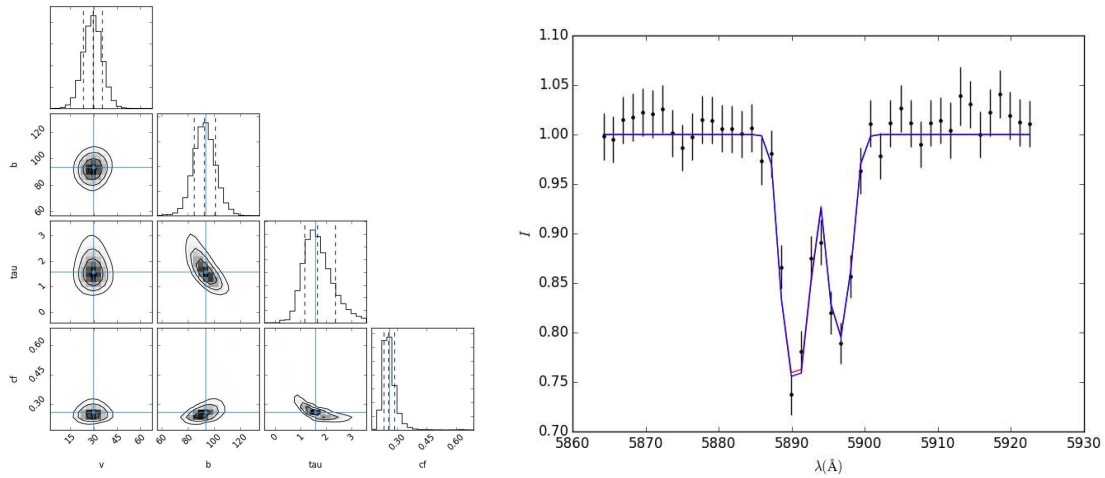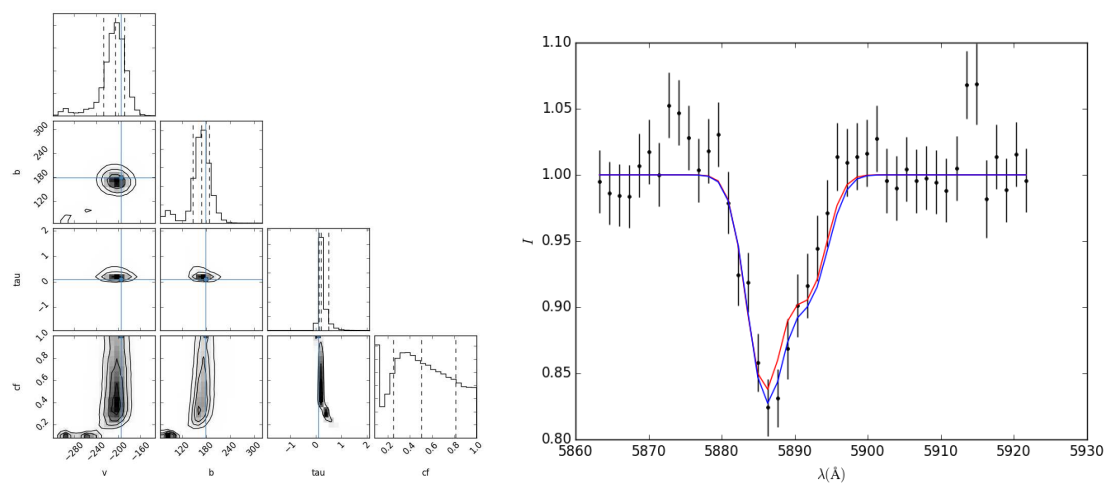
Fig. 3.6 Left: Example of a badly constrained parameter space for Seyfert galaxy, where the distributions of the parameters cannot be well approximated by means of Gaussians, making the parameter estimation somewhat ambiguous. Right: In blue the model corresponding to the MPFIT. Red line is model for the estimated from MCMC parameters.

Chapter 4

Results

In this section we present the results for the kinematics of the Na D excess for the galaxies in our sample and explore their dependence on a number of the properties of the host galaxies in order to better understand the origin of such an Na D absorption excess. Figure 4.1 shows the extracted relative Na D kinematics for the whole sample, that is, how the position and width of our best-fitting Na D profile compares to that of the stellar line-of-sight velocity distribution. In this $V_{\mathrm{NaD}} - V_\star$ vs $\sigma_{\mathrm{NaD}} - \sigma_\star$ diagram (or ΔV vs $\Delta\sigma$ in short) we can already isolate groups of galaxies, where the origin of the enhanced Na D absorption is likely different. To begin with, we note a group of objects with significantly blue-shifted Na D excess profiles ($\Delta V < -100\,\mathrm{km\,s^{-1}}$), that also tend be a bit broader than the stellar Na D lines (with $0 < \Delta\sigma < 100\,\mathrm{km\,s^{-1}}$). These are likely to be systems with truly outflowing gas, although this should be backed up by the presence of a considerable interstellar medium as traced by ionised-gas emission or reddening by dust. At the other end of the ΔV spectrum, there are a few galaxies where the Na D excess appears quite red-shifted, with $\Delta V > 100\,\mathrm{km\,s^{-1}}$, which may be indicative of inflows, if the Na D excess could indeed be ascribed to interstellar absorption. Yet, the red contours of Fig 4.1 indicate that by far most Na D profile show only a limited range of ΔV values, which is however biased towards slightly positive values. Among the bulk of our sample galaxies there are two distinct $\Delta\sigma$ behaviours. On one side, the majority of the galaxies show narrower σ_{NaD} values for the Na D excess component, which could be consistent with the presence of a well-settled gaseous disk whose kinematics would be necessarily colder than that of the galaxy stars. On the other hand, a smaller fraction of the objects with limited ΔV values show a more puzzling tendency for very broad Na D excess profiles, broader than the stellar Na D lines with $\Delta\sigma > 100\,\mathrm{km\,s^{-1}}$.
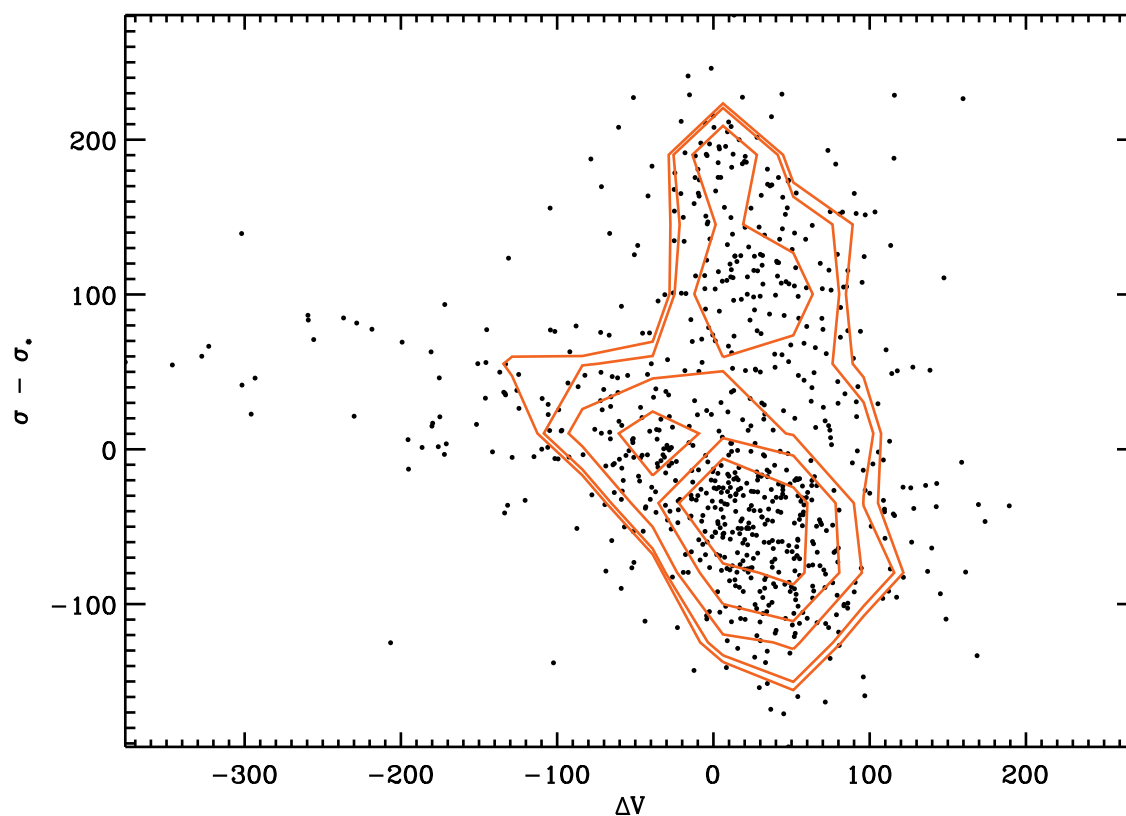
Fig. 4.1 For all galaxies in our sample, the relative velocity of the fitted Na D excess component with respect to the systemic galaxy velocity, ΔV, is plotted against the difference $\sigma_{NaD} - \sigma_{\star}$ between the width of the Na D excess and stellar velocity dispersion. The red contours trace the number density of galaxies in this diagram.
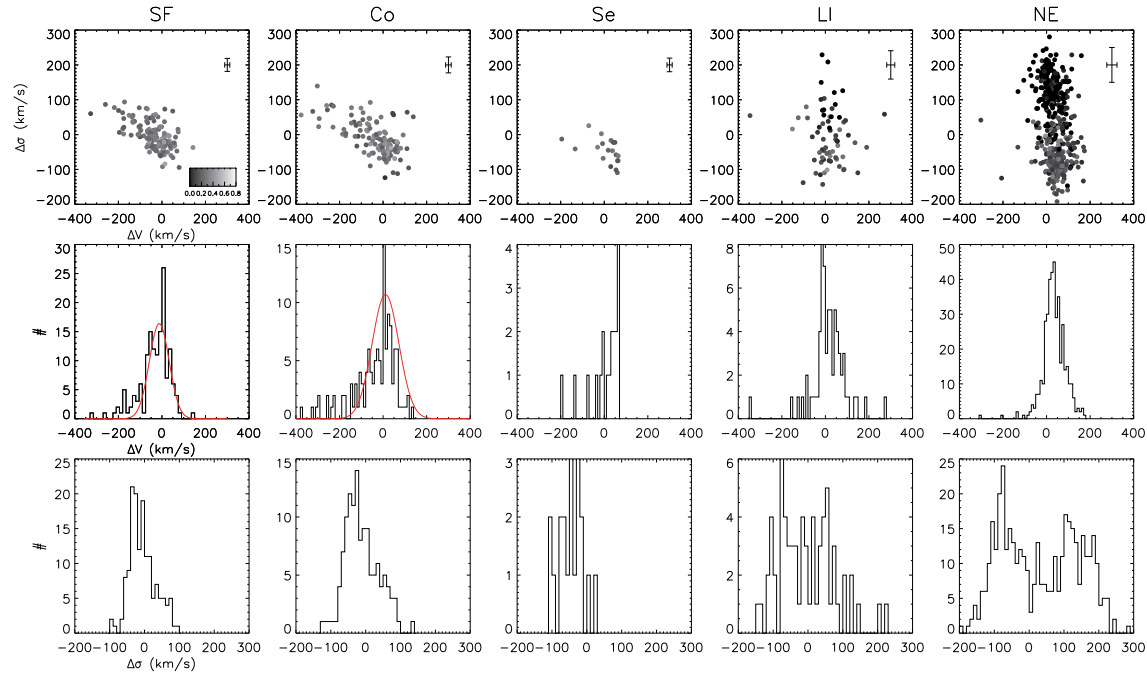
Fig. 4.2 Top: ΔV vs. $\Delta\sigma$ diagrams for different emission-line classes (SF = star-forming, CO = composite objects, Se = Seyferts, LI = LINERs, NE = no emission) and tracing also the reddening by dust, by color-coding the symbols using the OSSY $E(B - V)$ values. Middle and bottom panels: individual ΔV and $\Delta\sigma$ distributions for each emission-line class. The red curves in the middle panels for galaxies with star-forming and composite emission-line spectra show the best-fitting Gaussian to their ΔV distribution.

To shed more light on the origin of the Na D excess in our sample we can, first of all, ascertain whether the presence of reddening by dust and of nebular emission in the SDSS spectra indicates the presence of an interstellar medium, for indeed their absence would suggest that the Na D excess stems from stellar populations effects. If ionised-gas emission is present, we would further see, if there is any trend between nebular classification and the relative kinematics of the Na D excess. For instance, we may want to check whether star-formation, or AGN activity is observed, in objects displaying potential outflows in Fig 4.1. For this purpose, adopting the emission-line classification provided by Jeong et al., we have split our sample between quiescent objects, where there is little evidence of ionised-gas emission, and galaxies whose nebular emission is powered by OB-stars in star-forming regions, dominated by Seyfert AGN activity, or consistent with either LINER (Low-Ionisation Nuclear Emission Regions) emission, or a composite AGN and star-formation activity. Fig. 4.2 shows ΔV vs $\Delta\sigma$ diagrams for each of these emission-line classes, where we further color-code the symbols with different shades of grey, to trace the amount of reddening by dust in the stellar continuum. Fig. 4.2 immediately shows how the most blue-shifted Na D profiles occur always in objects with significant reddening by dust and nebular emission, thus confirming that these galaxies are potentially hosting galactic-scale outflows. On the other hand, most of the objects with only small ΔV values are found in galaxies with little or no ionised-gas emission, and among these, those objects with positive $\Delta\sigma$ values are almost exclusively found in galaxies with no reddening by dust. This further suggests that, in the latter cases, the Na D excess could be due to stellar population effects, such as an excess in the abundance of Na or in the number of low-mass stars that is not accounted by our model for the stellar spectrum. On the other hand, the presence of dust extinction in nearly all galaxies with $\Delta V \sim 0$ and $\Delta\sigma < 0$ would confirm the presence of relaxed gaseous disk, which may not always produce a detectable amount of ionised-gas emission.
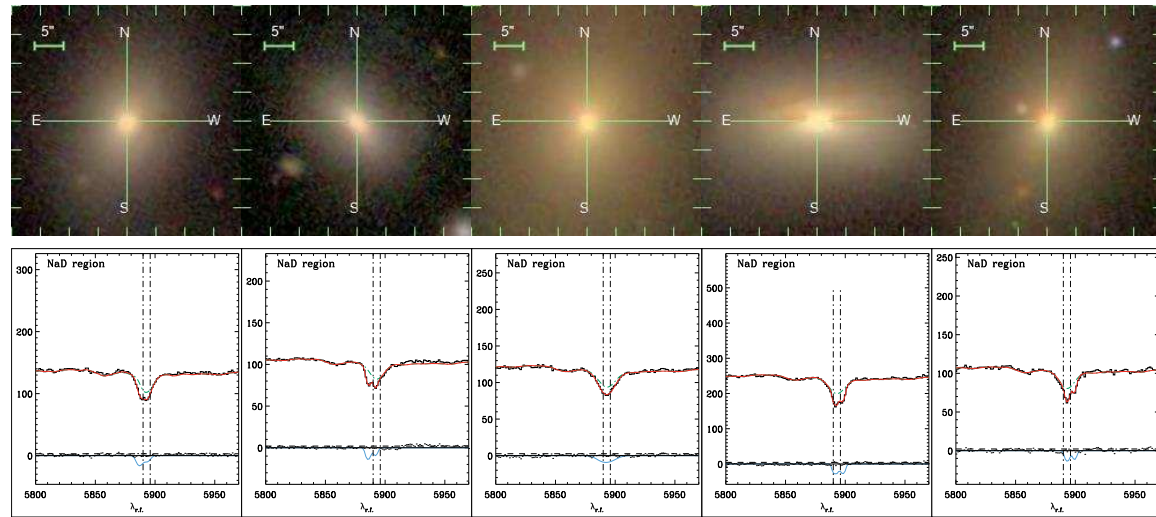
Fig. 4.3 Examples of early-type galaxies and of our fit in the Na D spectral region. The red line is the overall to the spectra, the green line is the contribution from the stellar-population template as matched by pPXF and the blue line is our fit to the additional Na D component.
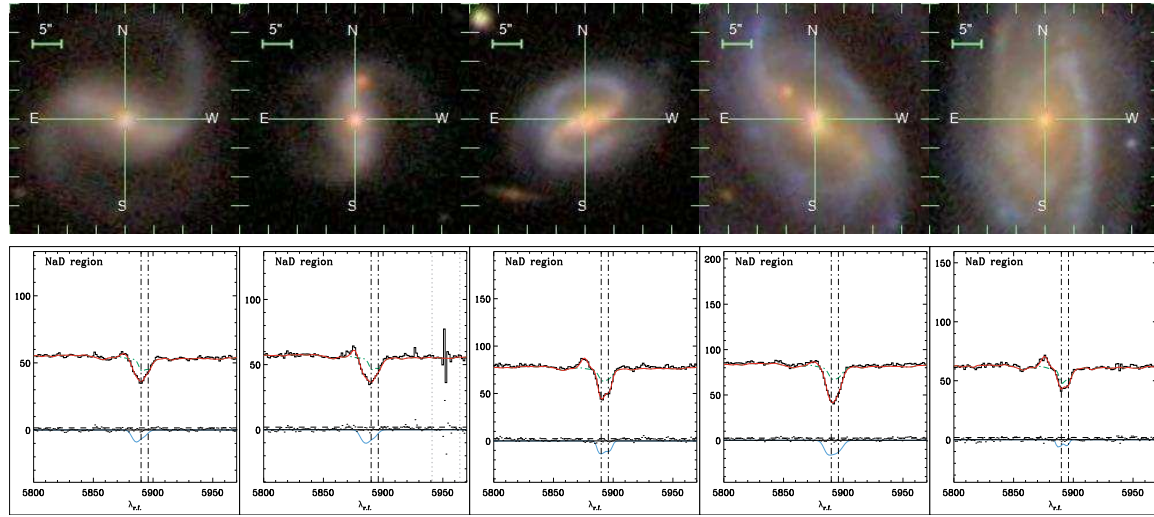
Fig. 4.4 Similar to Fig. 4.3, but now for late-type galaxies.

Inspecting the morphology of our sample galaxies further add to this puzzle. Figs. 4.3 and 4.4 show, respectively a few examples of early-type and late-type galaxies with Na D excess components, being blue- or red-shifted. We can notice that, in the case of the early-type galaxies, the presence of 'narrower' Na D spectral profiles coincide with the existence of a prominent dust lane in the galaxy, whereas outflows tend to occur in face-on spirals. These previous trends are consistent with the findings of Park et al. (2015), although in their analysis they only considered the relative velocity of the Na D excess profile, and only cursory consider its possible origin. In the following sections we further explore the nature of the Na D excess component as a function of the galaxy emission-line classification.

4.1   Quiescent Galaxies

The quiescent side of our sample consists largely of early-type galaxies (ETGs, 369 galaxies) and a few late-type galaxies (LTGs, 39). Of these, more than half are classified as 'peculiar' ETGs (pETGs, 212 objects) and LTGs (pLTGs, 33), as they generally show the presence of dust lanes (and sometime shells) in the case of ETGs or asymmetric features in LTGs (see Jeong et al. for visual examples of such classes). From Fig. 4.2 there no evidence of Na D outflows in quiescent objects. Instead, the ΔV distribution of the Na D excess profile appears centred around a small, but significant positive mean value of $\Delta V \sim 32\,\mathrm{km\,s^{-1}}$. Furthermore, the $\Delta \sigma$ distribution for quiescent objects displays a clear bi-modality, with a first group of objects with Na D profiles that are narrower than the photospheric Na D features and with $\Delta \sigma$ values peaking around $-100\,\mathrm{km\,s^{-1}}$ and a second group with broader Na D profiles where $\Delta \sigma$ typically extend between 100 and 200 $\mathrm{km\,s^{-1}}$.

As already noticed before, most of the quiescent objects, where the detection of reddening by dust indicates the presence of at least some interstellar medium, belong to the former group of galaxies, which in Fig. 4.2 show narrower Na D profiles and negative $\Delta \sigma$ values. This would suggest the presence of a relaxed dust system in these objects, most likely in the form of dust lanes as often observed in ETGs. Fig. 4.5 seems to back up this notion, since the quiescent dusty objects with narrower Na D profiles are generally classified as peculiar ETGs, which in turn indicates the presence of dust lanes according to Jeong et al. In fact, when taken per se, these dusty quiescent galaxies show an even more pronounced red-shift with a mean $\Delta V = 49\,\mathrm{km\,s^{-1}}$, suggestive of the presence of mild inflows in these dust-lane ETGs. This may relate to the fact dust lanes in ETGs are often due to the accretion of external gas (Sarzi et al. 2006), and thus in some cases may still be unsettled.

With regards to the quiescent objects with broader Na D profiles and $\Delta \sigma$ values between 100 and 200 $\mathrm{km\,s^{-1}}$, these are also generally devoid of dust and are more often classified as
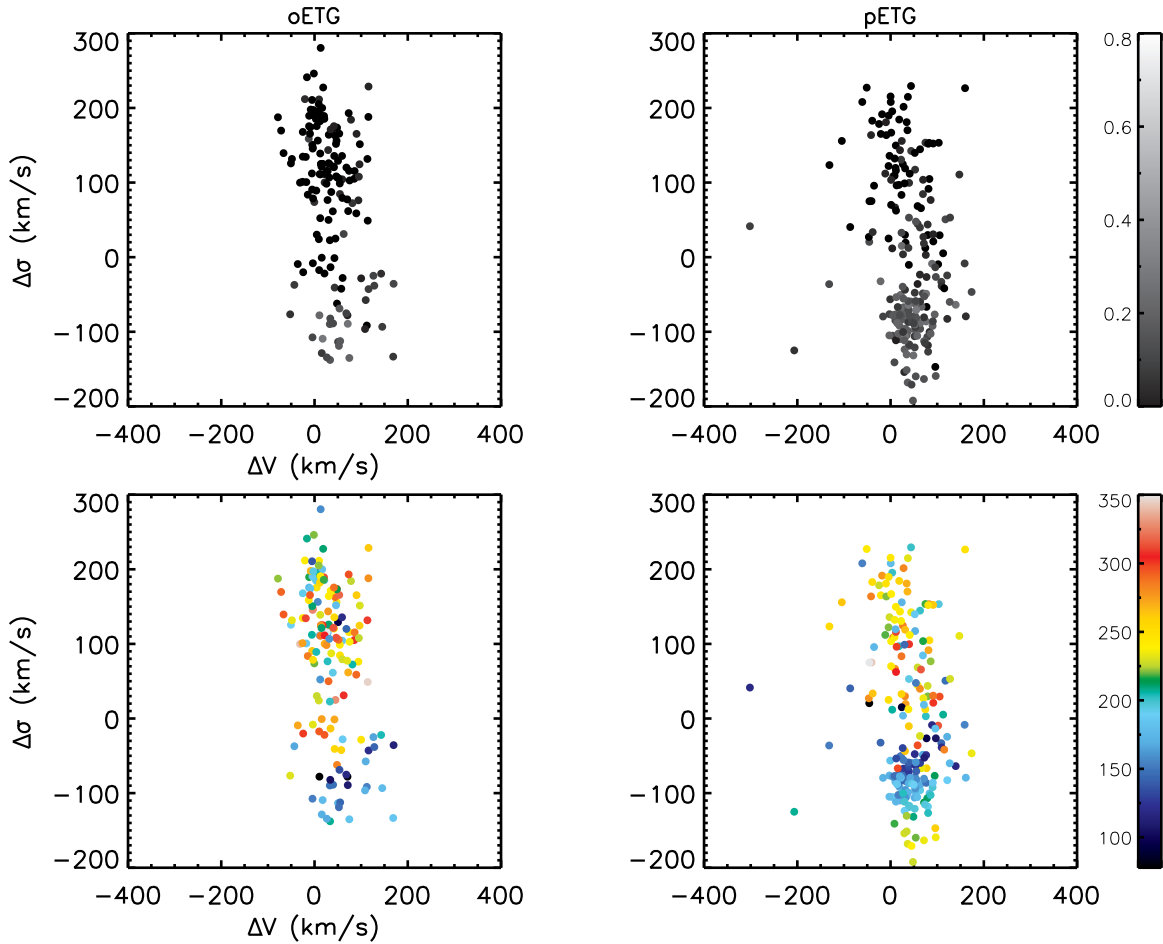
Fig. 4.5 Top panels: ΔV vs. $\Delta \sigma$ diagrams for the 'ordinary' and 'peculiar' early-type galaxies with little or no detected nebular emission, on the left and right panels respectively As in Fig. 4.2 the points are gray-coded by the observed reddening by dust, taken from the OSSY catalogue. The bottom panels the same ΔV vs. $\Delta \sigma$ diagrams but with symbols color-coded according to their the line-of-sight stellar velocity distribution $\sigma_\star$, which trace the dynamical mass of the system. By far, objects with low $\Delta \sigma$ are dusty objects classified as peculiar ETGs, thus containing most likely dust lanes. Conversely, the objects with $\Delta \sigma \sim 100 - 200 \, \mathrm{km \, s^{-1}}$ contains little or no dust, are more often classified as ordinary ETGs. They also show a wide distribution of $\sigma_\star$ that reaches up to the most massive systems in our sample, whereas peculiar and dusty ETGs are generally less massive.

ordinary ETGs. The absence of any indication of an interstellar medium strongly points to template-mismatch as the origin for the observed Na D excess. In turn, such a mismatch is likely associated either to an enhanced [Na/Fe] abundance or a stellar initial mass function (IMF) that is biased toward low-mass stars, which would not be currently accounted by the Bruzual & Charlot (2003) models on which our stellar population fit is based.

Super-solar [Na/Fe]>0 abundance or a bottom-heavy IMF would generally be expected in massive galaxies, as pointed by Jeong et al. and Conroy & Van Dokkum (2012a), so we ought to observe the same mass-dependency for the quiescent object with large $\Delta\sigma$ values. In this respect, Fig. 4.5 shows that the most massive quiescent ETGs, as traced by large values for their stellar velocity dispersion $\sigma_\star$, tend indeed to have the highest $\Delta\sigma$ values. On the other hand, objects with relaxed dust lanes and true interstellar Na D absorption are predominately lower-mass systems. In fact, among the latter objects we note a tendency for objects with larger $\sigma_\star$ values to stretch toward even smaller $\Delta\sigma$ values, which could simply reflect the tendency for the relaxed dust-lane systems to display rather constant σ_{NaD} values around $\sim 50 - 100 \, \mathrm{km\,s^{-1}}$.

Although the lack or ionised-gas emission or reddening by dust points to template mismatch as the origin of the Na D excess in quiescent ETGs with large $\Delta\sigma$ values, these considerations still do not offer an explanation for the fact that the fitted Na D excess profile appears broader than the stellar line-of-sight velocity distribution, and even a bit red-shifted. To try to understand the relative kinematics of an Na D excess due to either [Na/Fe] overabundance or the presence of a bottom-heavy IMF, in Fig. 4.6 we used the models of Conroy & van Dokkum (2012a) to show the impact on the Na D profile due to these two factors. More specifically we consider the case of a 13.5Gyr old stellar population and compute the ratio between models with a [Na/Fe]=0.3 and a Solar [Na/Fe]=0.0 pattern (black solid lines), both with the same Chabrier (2003) IMF, as well as the ratio between models with a bottom-heavy IMF (with a low-mass end logarithmic slope x=3) and again, a Chabrier IMF [1] (red lines). Such a division was done in order to mimic our procedure for measuring any possible interstellar Na D absorption, constrained in our investigation after normalizing our spectra by a reference model for the stellar continuum photospheric absorption. In all cases, the models where convolved at a common velocity dispersion of $300 \, \mathrm{km\,s^{-1}}$. In the case of pure [Na/Fe] overabundance the resulting Na D excess profile would be simply tracing a stronger absorption feature with a width comparable to the stellar velocity dispersion and no apparent blue- or red-shift. On the other hand, the Na D excess obtained by increasing

---

[1]The initial stellar mass function $\phi = \phi(m)$, where m is the stellar mass, is defined as a single power-law by Conroy & van Dokkum (2012a), with logarithmic slope of $x = -dln\phi/d\ln m$. Standard Chabrier (2003) and Salpeter (1955) IMFs come with low-mass end logarithmic slope of x = 1.8 and 2.35, respectively, whereas a value of x=3 would correspond to a bottom-heavy IMF.
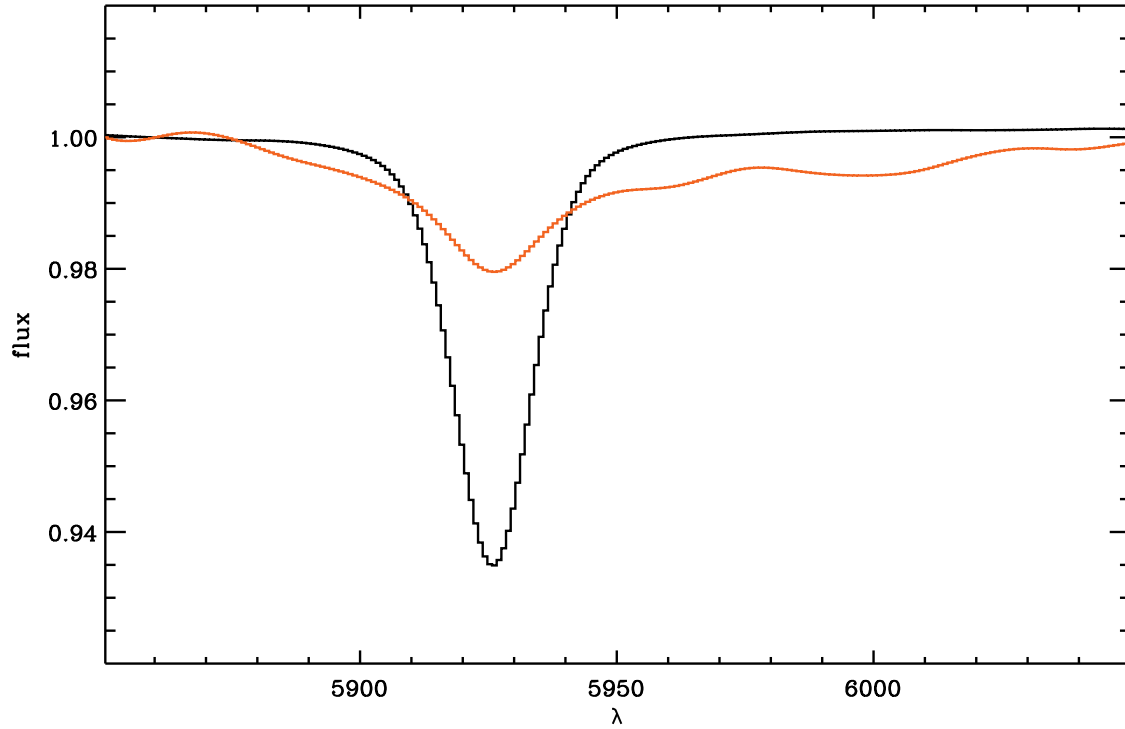
Fig. 4.6 Na D excess obtained by increasing the [Na/Fe] abundance (black line) and a bottom-heavy IMF (red line), while considering a 13.5 Gyr old stellar population. The impact of [Na/Fe] abundance was obtained by dividing Conroy & van Dokkum (2012a) for a Chabrier IMF and a [Na/Fe]=0.3 by a model with a Chabrier IMF and a Solar [Na/Fe]=0.0 abundance. Such a procedure is consistent with our analysis of our observed Na D excess profiles, where the former model spectra would mimic the data whereas the latter would represent our best, yet inadequate model for the stellar continuum. The impact of a more bottom-heavy IMF was obtained by dividing a model with a bottom-heavy IMF (with a low-mass end slope x=3 by the same reference model with a Chabrier IMF, after rescaling the latter model in order to account for the fact that models with much higher fraction of low-mass stars are much dimmer.

the relative fraction of low-mass stars would appear much broader, due to the higher surface gravity of such low-mass stars. Thus, even if [Na/Fe] overabundance and IMF variations were to work together, we speculate that just a small increase in the slope of the low-mass end of the IMF could still lead to a somewhat broader Na D excess, with high-velocity tails such that a Voigt profile would better reproduce the Na D profile as already noted by Park et al. (2015). In regards to the modest, but systematic, red-shift observed in quiescent objects without any dust absorption, we note that the Na D excess profile resulting from a bottom-heavy IMF also appears skewed toward longer wavelengths, which may also go some way towards explaining the observed red-shift. Whereas more detailed simulations are needed to quantitatively explain the position of truly quiescent objects in the ΔV vs. $\Delta \sigma$ diagrams, the relative kinematics of the template-mismatch Na D excess observed in these objects and the previous considerations provide an indirect additional evidence for a change in the IMF slope of ETGs.

4.2   Star-forming Galaxies

The star-forming objects in our sample show a much greater deal of reddening compared to quiescent galaxies, with a mean value of $E(B-V) \sim 0.27$ and consistent with the gas- and dust-rich nature of such a star-forming environment. In our sample star-forming galaxies are predominantly 'peculiar' LTGs (111 galaxies), with just a few pETGs (19) and ordinary LTGs (oLTGs, 19 objects). By fitting a Gaussian to the ΔV distribution for the Na D excess profile of star-forming galaxies (while fixing the standard deviation of such a Gaussian to that of the entire sample, or $60 \, \mathrm{km \, s^{-1}}$), Fig 4.2 highlights more quantitatively the presence of a 'tail' of objects with $\Delta V < -100 \, \mathrm{km \, s^{-1}}$ that are likely to host outflows.

Before proceeding to estimate the extent to which gas escaping from our star-forming galaxies, it is useful to check some expected trends with galaxy inclination for the best-fitting values of the parameters entering our fits to the Na D excess profiles. There is a considerable literature on Na D outflows in star-forming galaxies, from which in particular it emerges that outflows generally come with a bi-conical geometry with an opening angle between 45 and 60 degrees (Veilleux et al. 2005), so that outflows should not really be detectable in highly inclined systems. Furthermore, from the literature it is also clear that, should the quality of the data allow it, in spiral galaxies one ought to consider two distinct kinematic components, when fitting an Na D excess due to interstellar absorption: one at rest within the galaxy, representing the gas and dust in the disk and another, more blue-shifted component that is meant to capture the presence of a possible outflow (Chen et al. 2010). Fig. 4.7 shows our best-fitting parameter as a function of inclination only for late-

type star-forming objects, for which we can infer an inclination. This was obtained using the a/b axis-ratio `expAB_r` of the best SDSS-pipeline fit to a galaxy surface-brightness profile with an exponential law, and then simply using $i = 180°/\pi \arccos(b/a)$. Consistent with the previous expectations, we observe a trend for increasing outflow velocities (i.e. decreasing ΔV) in galaxies that are more face-on. Conversely we find no outflows in very inclined systems, for $i \sim 70°$ or above, where our single kinematic component fitting is almost certainly capturing the Na D insterstellar absorption from material orbiting in the disk of these galaxies. In Fig. 4.7 there is also a number of objects with high outflow velocities with inclinations in the $45 - 60°$ range, where the contribution of the systemic and outflow component should become comparable (Chen et al. 2010). This may be due to the fact that the outflowing material does not generally fill the bi-conical outflowing structure, but rather accumulates at its edges, which could cause us to pick a strong outflow velocity signal when such edges are subtended by our spectral aperture. Interestingly, the broadest Na D profiles are also observed in this inclination range, presumably because our single component fit adjusts itself to pick up the comparable signals from both the systemic and outflow components. No particular trend is observed for the covering factor or the optical depth as a function of inclination, but then again our estimate of these strongly correlated parameters is considerably cruder and sometime does not even converge (as indicated by the many instances where $C_f = 1$).

To estimate the fraction of gas that is likely to escape from our sample galaxies we need give an order of magnitude estimate of the escape velocity V_{esc} and to assume some geometry for the gas flow. Since our spectroscopic observations concern only the regions encompassed by the 3"-wide SDSS fiber, the most conservative way to estimate escaping gas fraction is to assume that most of gas is taking off from the edges of these regions and to compare the observed Na D velocities to the V_{esc} value that is needed to escape from the whole mass M_{dyn} inside these regions. Assuming a spherical geometry for the mass distribution subtended by the SDSS fiber, appropriate when looking down at the bulge-dominated regions of disk galaxies or at early-type galaxies, a reasonable approximation to the escape velocity of material at a distance r from the center is given by $\sqrt{2GM_{dyn}/r}$, where G is the universal gravitational constant and M_{dyn} is total mass inside the radius r. In the case of elliptical and lenticular galaxies, Cappellari (2013) provides a robust estimate for M_{dyn}, as $M_{dyn} = 5.0 R_e \sigma_\star^2/G$, where R_e is the half-light radius of the galaxy and $\sigma_\star$ is the observed stellar velocity dispersion. As we are interested only in the escape velocity from the mass enclosed within the regions encompassed by our SDSS fibers, we can set $r = R_e$ in the previous expressions and obtain an estimate of the escape velocity that is independent of such radius. Indeed, by combining them we find that $V_{esc} = \sqrt{10}\sigma_\star$, where $\sigma_\star$ is simply
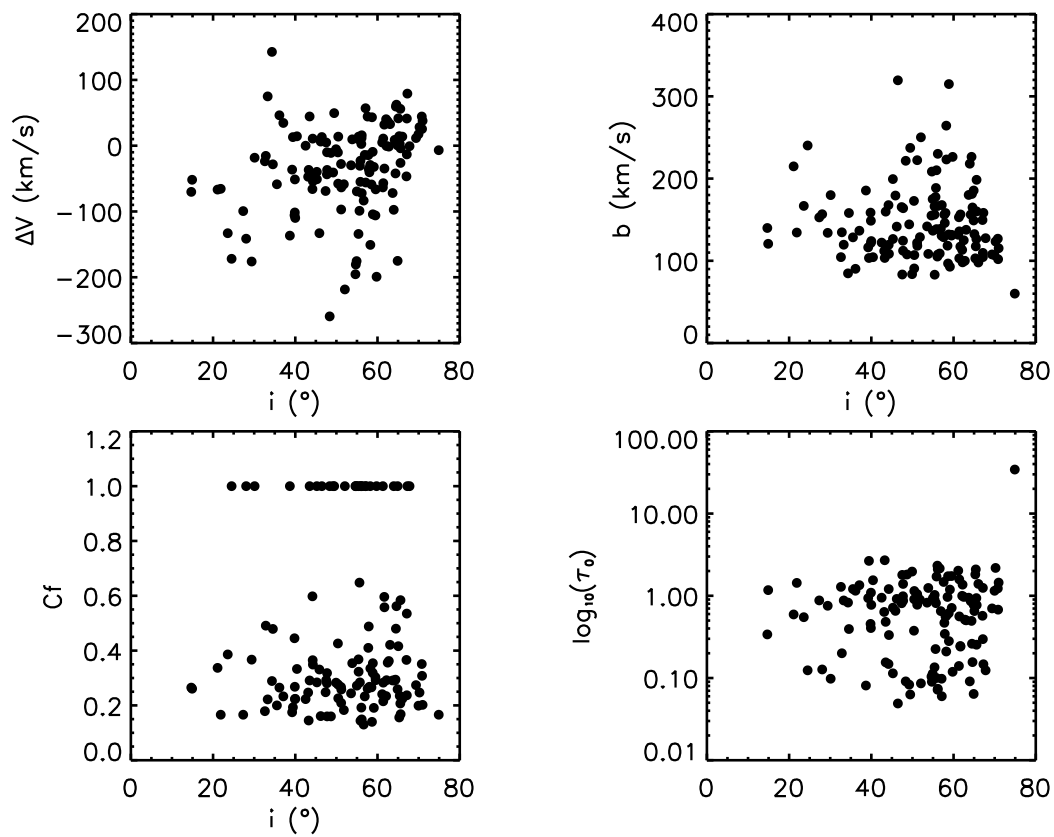
Fig. 4.7 Retrieved best-fitting profile parameters for the late-type star-forming galaxies as function of inclination, where $i = 0°$ and $90°$ correspond to the face-on and edge-on systems, respectively.
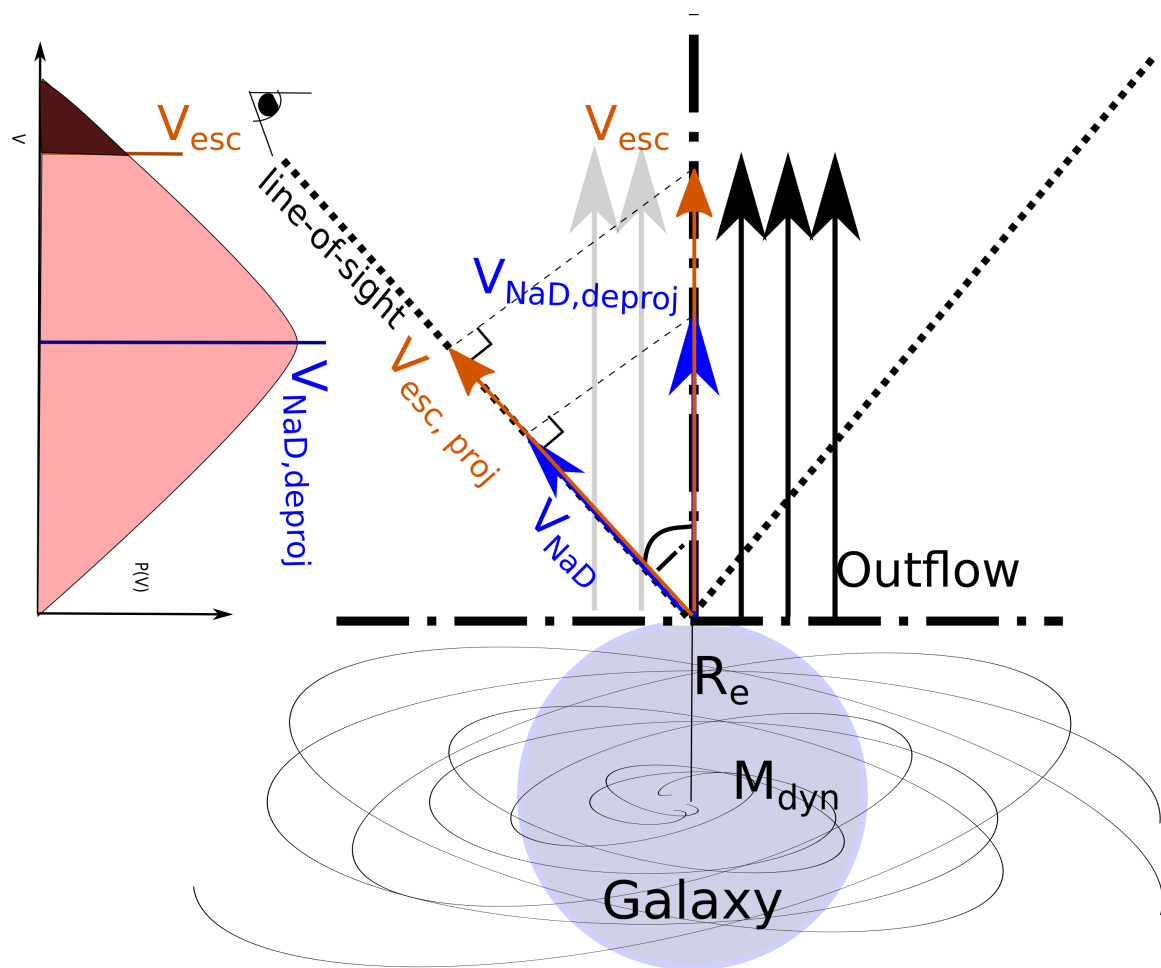
Fig. 4.8 The assumed geometry, described in sec. 4.2.

the stellar velocity dispersion measured from the SDSS spectra themselves. Clearly, when looking only at the central regions of nearby galaxy, gas velocities exceeding our estimated values of V_{esc} do not strictly imply the gas would escape the entire galaxy, whereas such case is more plausible for the most distant objects, where the SDSS fiber covers a much larger fraction of the galaxy. This may also apply to distant disk galaxies, since the Cappellari et al. formula will still capture most of the dynamical mass by means of the $\sigma_\star$ values, even though it will also trace the rotation of the stars in the stellar disk.

Now, given these assumptions, as a first, but conservative guess for identifying systems, where gas is likely to be escaping at least from the central regions, we tag as 'strong outflows' those systems, where the observed relative Na D velocity ΔV already exceed our estimate for V_{esc} (that is, where for blue-shifted objects $|V_{NaD}| > V_{esc}$). On the other hand, for LTGs we can assume that the gas flows perpendicularly to the disk (fig. 4.8) and deproject the observed relative Na D velocity ΔV by dividing it by the cosine of the inclination, since $V_{NaD} = V_{depr,NaD} \times \cos i$. By comparing $V_{depr,NaD}$ to V_{esc} we can estimate a fraction for the gas that is actually escaping using our assumption of Gaussian line-of-sight velocity distribution for the Na D absorbing clouds. In fact, we can carry out the same exercise by comparing the observed Na D velocity ΔV with a projected estimate for the escape velocity $V_{esc,proj} = V_{esc} \times \cos i$ along the line-of-sight. Under such assumptions, the fraction of gas escaping, the gravitational potential well, would be given by the expression:

$$r_{esc} = \int_{Vesc}^{\infty} \frac{1}{\sqrt{2\pi}\sigma_{NaD}} e^{-(V-V_{NaD})^2/2\sigma_{NaD}^2} dV \tag{4.1}$$

Based on the two values of $Vesc$ and V_{NaD} this integral has two solutions:

$$r_{esc} = \begin{cases} 0.5 + erf(\frac{V_{NaD}-Vesc}{\sigma}), V_{NaD} > Vesc \\ 0.5 - erf(\frac{Vesc-V_{NaD}}{\sigma}), V_{NaD} < Vesc, \end{cases}$$

where the 'erf' is the so-called error function.

Fig. 4.9 points to objects with 'strong outflows' and shows the escaping fraction of the gas by color-coding the symbols that correspond to LTGs with an inclination of less than $45°$, since we do not expect to detect outflows anyway for more inclined systems. For ETGs, the color-coding is done without applying any correction to V_{esc}, and thus represent only lower-limits for the fraction of escaping gas. Among the color-coded points, we tag as 'mild outflows' those objects where the escaping fraction is greater than 16%. Fig. 4.9 also shows that the strength of the Na D excess, per se, does not correlate with the retrieved Na D kinematics. Thus, for instance, a stronger Na D absorption does not imply an Na D outflowing system. Finally, as one would expect, Fig. 4.9 confirms that outflows are more
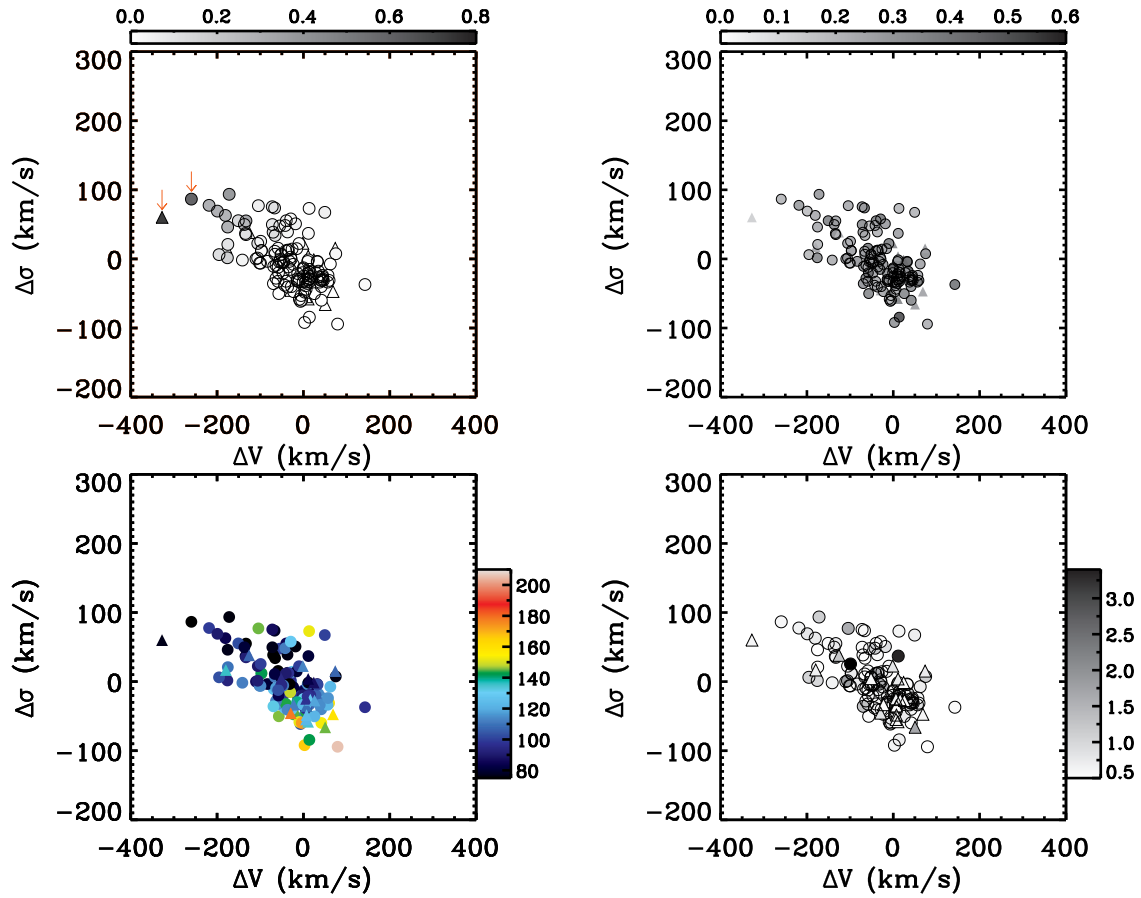
Fig. 4.9 Various forms of the ΔV vs. $\Delta\sigma$ diagram for star-forming galaxies, color-coded by a) fraction of escaping gas (top left, see text for details), b) reddening by dust (top right, from the OSSY catalogue as in Fig. 4.2), c) by stellar velocity dispersion as a tracer of dynamical mass (bottom left) and d) by the value of the f_{NaD} parameter of Jeong et al. The red arrows point in the top left panel indicated galaxies likely to host 'strong outflows', where the Na D lines are blue-shifted and $|\Delta V_{NaD}| \geq V_{esc}$.

easily triggered in low-mass systems, although this appears to be only a necessary, but not sufficient condition.

In our star-forming subsample there are only two cases of 'strong outflows' and 8 cases of 'mild outflows', where generally speaking the latter can occur in galaxies with $\Delta V < -50\,\mathrm{km\,s^{-1}}$ whereas the former happen only when $\Delta V < -100\,\mathrm{km\,s^{-1}}$. Previous studies, based on luminous or ultra-luminous infrared galaxies, reported much higher fraction of outflowing galaxies of around 50% (Rupke et al. 2005b,a). Yet, although we also notice a minimum threshold of specific star-formation activity for triggering the outflows, as traced by a minimum EW for the Hα emission of 20Å, we note that the IR-luminous galaxies come with a much higher rate of star formation than the ones in our sample. Also, the distance

redshift cut, built-in our sample, may have precluded us from covering a substantial fraction of such rare IR-bright systems.

4.3   Composite Galaxies

The objects, classified as composite, show a superposition of star-bursting and AGN activity in their emission-line SDSS spectrum. More than half of them are pLTGs (85) with 14 oLTGs, 26 pETGs and 1 oETG. Composite objects show a rather similar distribution to the star-forming galaxies in the ΔV vs. $\Delta\sigma$ diagrams of Fig. 4.2, with a similar tail of objects with blue-shifted Na D profile. The first question that therefore arises, is to what extent are the ΔV and $\Delta\sigma$ distribution of the composite and star-forming galaxies consistent with each other.The observed similarity is not completely unexpected, given that composite nuclei are most often observed in disk galaxies. Furthermore, if the ΔV and $\Delta\sigma$ distribution are indeed similar, this would be suggestive that AGN play little or no part in driving the outflows in composite objects, leaving instead this role to circum-nuclear star-formation. Before tackling this question, however, we need to make sure that these two kinds of nebular activity occur in similar objects, also viewed under a similar distribution of inclinations. To check for this we use the two-sided Kolmogorov-Smirnov statistic test (Press et al. 1986, K-S test) to compare the absolute r-band magnitude distribution of these two subsamples, and in the case of LTGs, also the distribution of inclination values (derived as described in the previous section). Indeed, both these quantities are relevant, when it comes to the ability of a galaxy to retain its gas and our capacity to detect outflows, considering that the r-band absolute magnitudes traces the total stellar mass of a galaxy. According to the K-S test there is a 99% probability the absolute r-band magnitude and inclination distributions of the star-forming and composite galaxies are drawn from the same parent distribution, with K-S statistic of 0.026 and 0.032 respectively. Having established this point, we compare both the single ΔV and $\Delta\sigma$ distributions of these two groups of galaxies using the same K-S test, or even compare directly the two-dimensional ΔV vs. $\Delta\sigma$ distribution using the two-dimensional version of the same test. Individually, the ΔV and $\Delta\sigma$ distribution are not likely drawn from the same parent distribution with a probability $\sim 1.28\%$ (K-S statistic=0.189358) and $\sim 16.43768\%$ (K-S statistic=0.133216). The same holds also for the two-dimensional test, where this probability is $\sim 1.6\%$. Furthermore noting that the K-S test is not specifically tailored to distributions with 'tails' such as the observed ΔV distribution, we further applied the Kuiper test (Press et al. 1986), but also in this case the returned probability that the ΔV distributions were drawn from the same parent distribution is still just $\sim 5\%$ (Kuiper statistic: 0.207201).
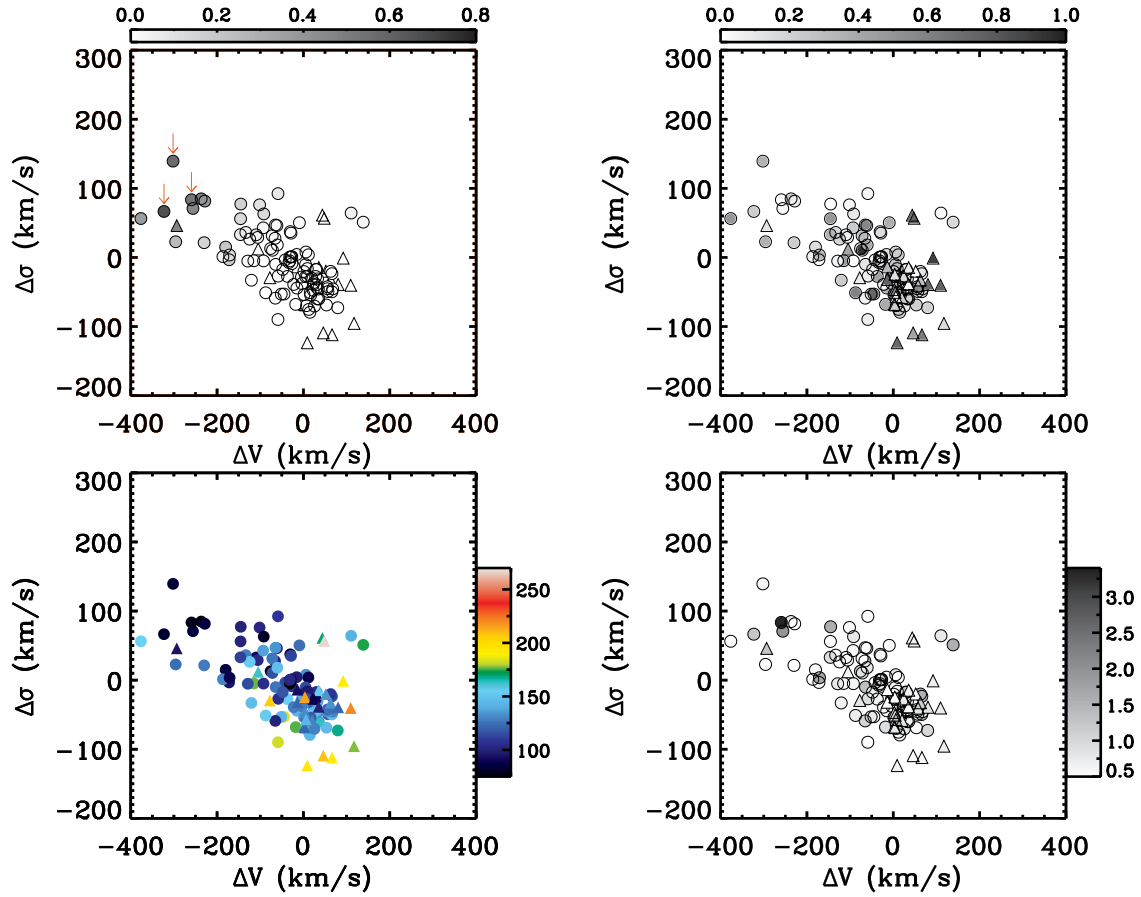
Fig. 4.10 Various forms of the ΔV vs. $\Delta\sigma$ diagram for galaxies with composite AGN/star-forming central emission, color-coded by a) fraction of escaping gas (top left), b) estimated fraction of the emission powered by the AGN (top right, see § 4.3), c) by stellar velocity dispersion as a tracer of dynamical mass (bottom left) and d) by the value of the f_{NaD} parameter of Jeong et al. The red arrows point in the top left panel indicated galaxies likely to host 'strong outflows', where the Na D lines are blue-shifted and $|\Delta V_{NaD}| \geq V_{esc}$.

Comparing the ΔV distribution of composite and star-forming galaxies, most likely these tests convey the fact that a larger fraction of composite objects seems to fall in the tail of blue-shifted Na D excess profiles, extending also to more negative ΔV values. Since in these objects star-formation is accompanied by AGN activity, a legitimate second question would be to see, if the presence of the AGN is responsible for boosting the fraction of blue-shifted objects. To answer this question we proceed to estimate the AGN contribution to the optical emission of our composite objects, in order to check, if a stronger fraction of AGN-powered emission correlates also with a greater gas escape fraction. To estimate the 'AGN fraction' in our composite objects we place them in the same emission-line ratio diagnostic diagrams that were used by Jeong et al. to classify in the first place the nebular emission (i.e. the diagram juxtaposing the [NII]/Hα and [OIII]/Hβ line rations), and further proceed to estimate their distance d_{AGN} to the extreme theoretical dividing line between the star-bursts and AGN of Kewley et al. (2001) and their distance d_{SF} to the purely star-forming limit of Kauffmann et al. (2003). The ratio $r_{SF/AGN} = d_{SF}/(d_{SF} + d_{AGN})$ would then serve as an indication of the AGN fraction. Fig. 4.10 shows that objects with a more blue-shifted Na D excess profiles, or a higher percentage of outflowing gas, do not have a larger AGN fraction. Instead, composite objects, mostly powered by AGN activity, are mainly found in systems with little or no Na D blue-shift. This is indicative that outflows are primarily driven by star-formation in composite objects, and either that star-formation is weaker in objects that are dominated by AGN activity, or the latter occur more often in the most massive systems, where driving outflows is more difficult anyway. Similar to the case of star-forming objects, we also find no correlation with the f_{NaD} index and that objects with strongly blue-shifted Na D profiles do not occur preferentially in the least massive galaxies.

Overall, in our composite objects subsample there are three cases of 'strong outflows' and 9 cases of 'mild outflows', both only marginally more frequent than found in the star-forming sub-sample. Although both based on IR-luminous-selected samples, the studies of Rupke et al. (2005b) and Sell et al. (2014) also find that among their sample galaxies with central composite emission, outflows appear mostly driven by star-formation, with no significant enhancement of the outflow velocities as a function of estimated AGN fraction.

4.4   LINER Galaxies

The galaxies, displaying ionised-gas emission consistent with LINER emission, are predominantly ETGs (31 pETGs, 14 oETGs), as expected given that LINERs are typically found in this kind of systems. We also find LINERs in 4 oLTGs and 18 pLTGs, likely to be bulge-dominated systems or objects with a lower fraction of gas, since LINERs are also typically

found in objects with less important interstellar components (see Ho (2008) for a review). It should be further emphasised that the presence of LINER-like activity does not necessarily imply the presence of AGN activity. LINER-like emission can also arise from diffuse gas powered by other mechanisms, such as shocks or old UV-bright stars (Sarzi et al. 2010, e.g.) in our particular cases of distant galaxies, where the spectroscopic fibre would subtend large fraction of the host galaxy. The lack of a rich ISM in LINERs provides an explanation as to why there is not a great number of them, showing an Na D excess and thus part of the Jeong et al. sample, despite LINERs being fairly common in the OSSY catalogue.

The relative kinematics of the Na D excess in LINERs Fig. 4.2 show that these objects are distributed in the ΔV vs. $\Delta\sigma$ diagrams in a fashion rather like the galaxies with little or no ionised-gas emission. Given the fact that LINERs are found mostly in ETGs and in objects that do not have a great deal of interstellar medium, the Na D excess profile could - similar to the case of quiescent galaxies - arise in a large part from template mismatch. For LINERs, where the Na D excess is truly interstellar in nature, we expect most often to find a rather relaxed gaseous system, given that most LINERs effectively consist of extended gas emission, instead of AGN emission. Although the quiescent subsample is more largely dominated by ETGs, in terms of absolute r-band magnitudes and inclinations for LTGs (which are most relevant in terms of our detection capability) the quiescent and LINER sample are consistent with having been draw from the same parent distribution, at a 99% probability level according to K-S tests. It does, therefore, make sense to compare the ΔV vs. $\Delta\sigma$ diagrams of these two subsample. Using both the one and two-dimensional K-S tests as done in the previous two sections, we find that there is only a negligible possibility that both LINERS and quiescent galaxies were drawn from same parent distribution when it comes to there relative Na D excess kinematics, in particular when it comes to the $\Delta\sigma$ distributions where LINERs do not show the same pronounce bi-modality as observed in quiescent objects. Still we can recognise also in LINERs a tendency for objects without much reddening to display large $\Delta\sigma$ values, so clearly stellar-population effects most likely enter in the Na D excess profile of many LINERs.

With the mixed nature of LINERs, it is worth investigating whether the objects with true AGN emission behave somewhat differently in the ΔV vs. $\Delta\sigma$ diagram. For this we can used the criterion, designed by Cid Fernandes et al. (2011), to separate true AGN LINERs from LINER-like emission galaxies. The LINER-like emission is generally powered by diffuse ionised-gas emission, not the AGN. A distinction is made knowing the former can only produce relatively weak lines with a limiting EW of Hα of 3Å. Figure 4.11 show position of galaxies with true AGN LINER emission and the derived fraction of escaping gas for our LINERs, which in most case are merely lower-limits given that most of these

objects are ETGs. True AGN LINERs tend to reside in the lower part of the ΔV vs. $\Delta \sigma$ diagram, dominated by lower-mass systems, where the presence of dust lanes is most likely. The escape fractions are pretty low among LINERs. The gas is probably escaping for only one object, where incidentally we also find true AGN emission.

Overall, in our LINER subsample we find only one case of 'strong outflow' with no instances of 'mild outflows'. Although for many LINERs the escape fractions are just lower limits, the derived escape fractions are so low ($< 1\%$) that even 'mild outflows' are quite unlikely. At odd with these results, in their study, Rupke et al. (2005a) report identical detection rate of outflows amongst the star-forming and LINER galaxies. The sample of Rupke et al. consists, however, of explicitly selected IR-luminous galaxies and it is likely that despite the presence of central LINER AGN, most of their galaxies are permeated by star-formation, which in turn might be responsible for driving their observed outflows. In fact, we note that the spectral data of Rupke et al. do not necessarily cover the same central regions when the LINER activity has been reported. On the other hand, when using SDSS data consistently subtending the same regions when probing the nebular emission and the Na D absorption, in Sarzi et al. (2016, see Appendix A) we found that LINERs emission is never associated with Na D outflows.

4.5   Seyfert Galaxies

Nearly all the galaxies, in our sample, showing Seyfert central activity are classified as 'peculiar' - 7 pETGs, 11 pLTGs, and only one oETG showing no morphological disturbance. Seyfert galaxies seem mostly concentrated in the low $\Delta \sigma$ region of the ΔV vs. $\Delta \sigma$ diagrams of Fig. 4.2, with just a couple of objects with Na D excess profile that are blue-shifted by more than $100 \ \mathrm{km \ s^{-1}}$ with respect to the galaxy rest-frame. The ΔV and $\Delta \sigma$ distributions of Seyfert galaxies resembles more that of the star-forming and composite objects, but in detail the K-S tests exclude that Seyferts were draws from common parent samples of either class of objects.

Using our standard fitting techniques for matching the Na D excess profile, Fig. 4.12 shows that there are basically neither 'strong' nor 'mild outflows' among the galaxies hosting a Seyfert AGN. The lack of outflows would therefore suggest that optical AGNs are not capable of driving substantial galactic winds on the physical scales typically subtended by our SDSS observations (i.e. 0.4 to 4 kpc), although we also notice that Seyfert activity also takes place in galaxies that are generally more massive, in comparison to the star-forming and composite subsamples.
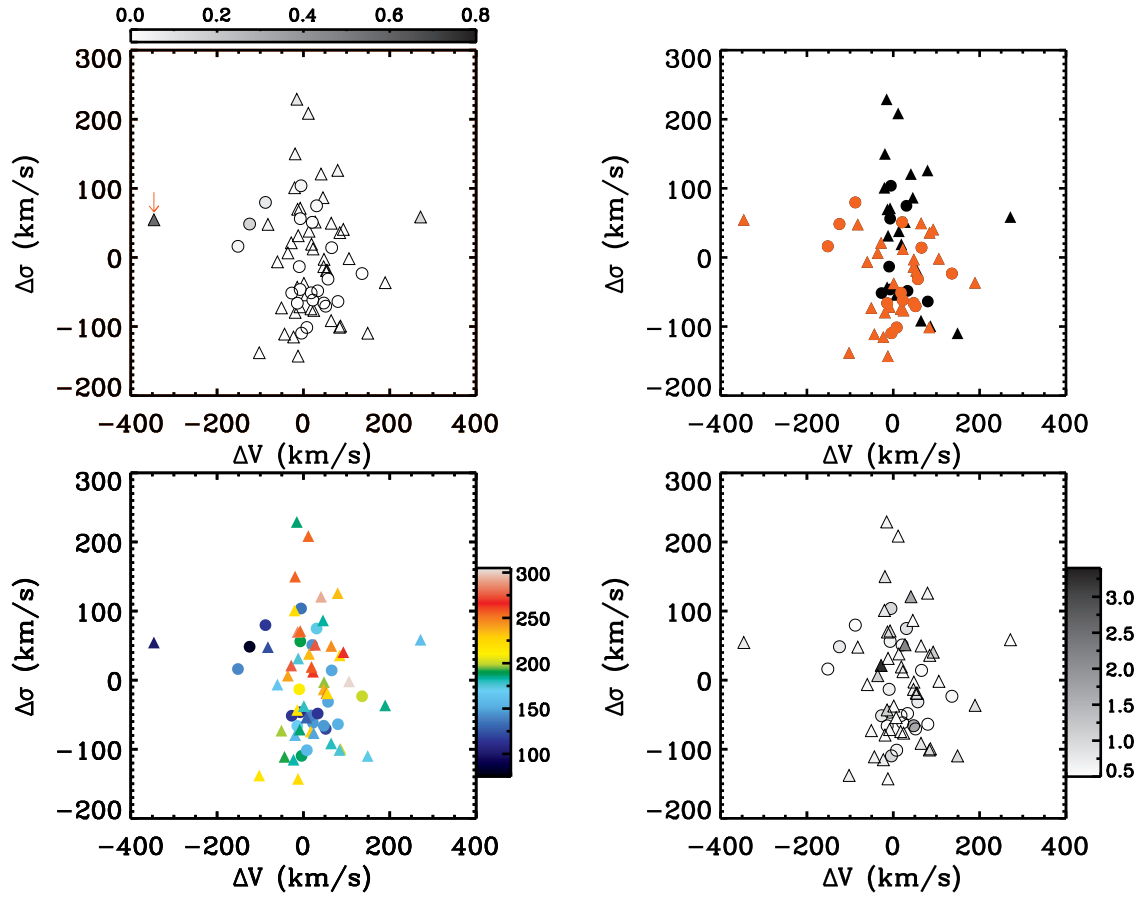
Fig. 4.11 Various forms of the ΔV vs. $\Delta \sigma$ diagram for galaxies with LINER-like central emission, color-coded by a) fraction of escaping gas (top left), b) presence of true AGN LINER emission (top right, shown by the orange points), c) by stellar velocity dispersion as a tracer of dynamical mass (bottom left) and d) by the value of the f_{NaD} parameter of Jeong et al. The red arrows point in the top left panel indicated galaxies likely to host 'strong outflows', where the Na D lines are blue-shifted and $|\Delta V_{NaD}| \geq V_{esc}$.
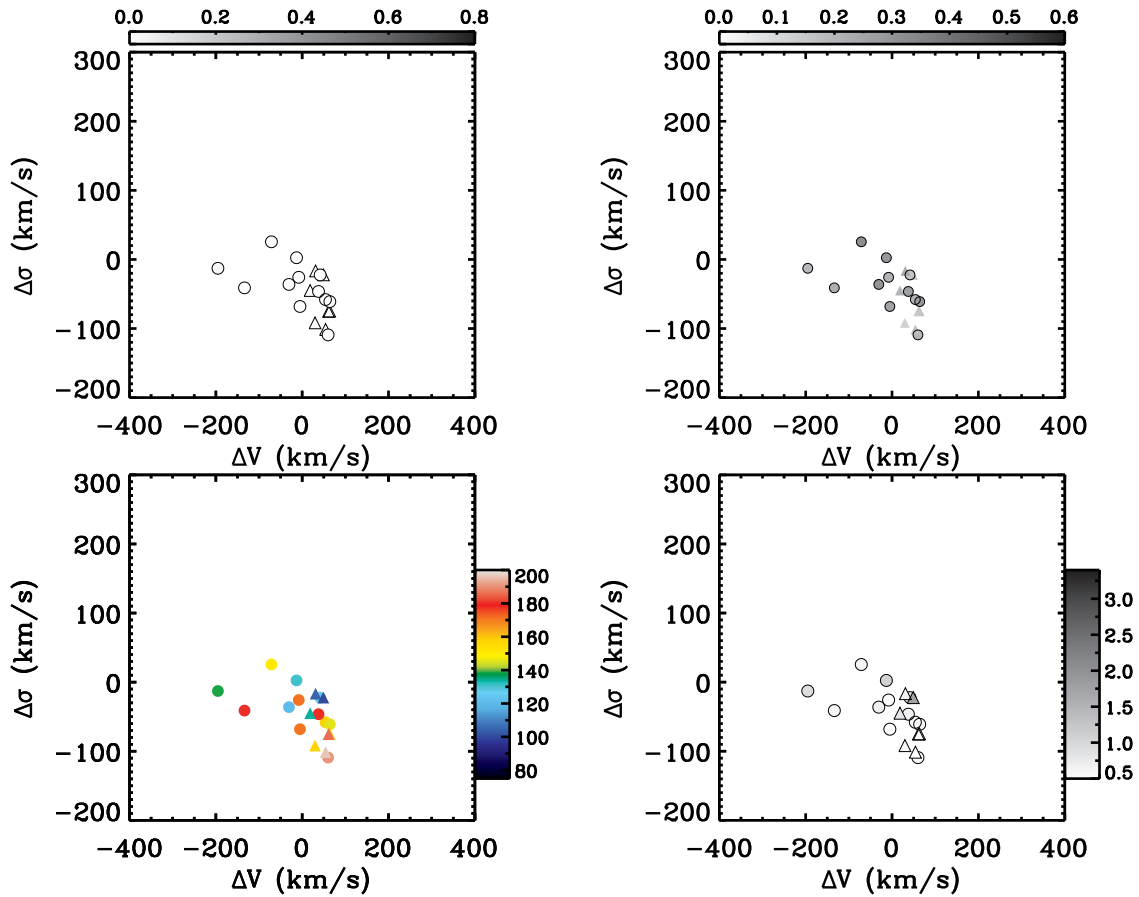
Fig. 4.12 Various forms of the ΔV vs. $\Delta\sigma$ diagram for galaxies dominated by Seyfert emission, color-coded by a) fraction of escaping gas (top left, see text for details), b) reddening by dust (top right, from the OSSY catalogue as in Fig. 4.2), c) by stellar velocity dispersion as a tracer of dynamical mass (bottom left) and d) by the value of the f_{NaD} parameter of Jeong et al. The red arrows point in the top left panel indicated galaxies likely to host 'strong outflows', where the Na D lines are blue-shifted and $|\Delta V_{NaD}| \geq V_{esc}$.

Because of the low number of Seyferts, the interesting nature of these objects, and to verify our previous fitting technique, we decided to perform a Bayesian model fitting, for all of the Seyfert galaxies in our sample, including back also the additional 4 objects, previously excluded based on a low quality fit using our standard MPFIT-based approach. As described in §3.3 we ran a Markov Chain Monte Carlo simulation to fit the previously described line profile. We adopt the prior distributions for the model parameters to have uniform probability density with the same limits as we used for our MPFIT-based approach, namely: $0 \leq \tau_0 \leq 1000$, $0 \leq C_f \leq 1$, $-700 \leq v_{NaD} \leq 700$, and $40 \leq b_D \leq 700$. We fitted the same model, previously described. Only the uncertainties from the SDSS spectrum in just one dimension- the flux were used. No errors in the measurements for the wavelength were incorporated in our fitting procedure. The log-likelihood $\mathcal{L} = -\frac{1}{2}\chi^2$ was incorporated to generate the posterior distributions of the parameters in our model. The best-fitting values for the parameters were obtained by taking the 50th percentile (i.e. the median) of the posterior distributions. To estimate the errors on the best-fitting parameters we took the 68% credibility level on the retrieved posterior distributions from the MCMC simulations for the σ_{NaD} and ΔV. The final MCMC-based best-fitting values for ΔV and $\Delta\sigma$, together with their 68% credibility levels are shown in Fig. 4.13. Comparing Fig. 4.13 with Fig. 4.12 we find there no great difference in the final best-fitting values for ΔV and $\Delta\sigma$ for the Na D excess profiles, retrieved either by our standard approach or by using the MCMC simulations, confirming our previous conclusions on the presence of outflows in Seyferts.

In their IR luminous sample Rupke et al. (2005b) found that objects with central Seyfert activity and those entirely dominated by star-formation were equally likely to host outflows. This is not entirely surprising, as the considerations made in the case of LINERs would also apply here in the case of Seyferts. In fact, when focussing on more regular, IR-faint Seyfert galaxies, Krug et al. (2010) report only small detection rate of outflows ($18 \pm 9\%$), closer to our results and also the ones reported in Sarzi et al. (2016). Interestingly, like us Krug et al. also find that most of their Seyfert galaxies show a red-shifted absorption, which they ascribed to the possible presence of dust lanes and infalling gas.
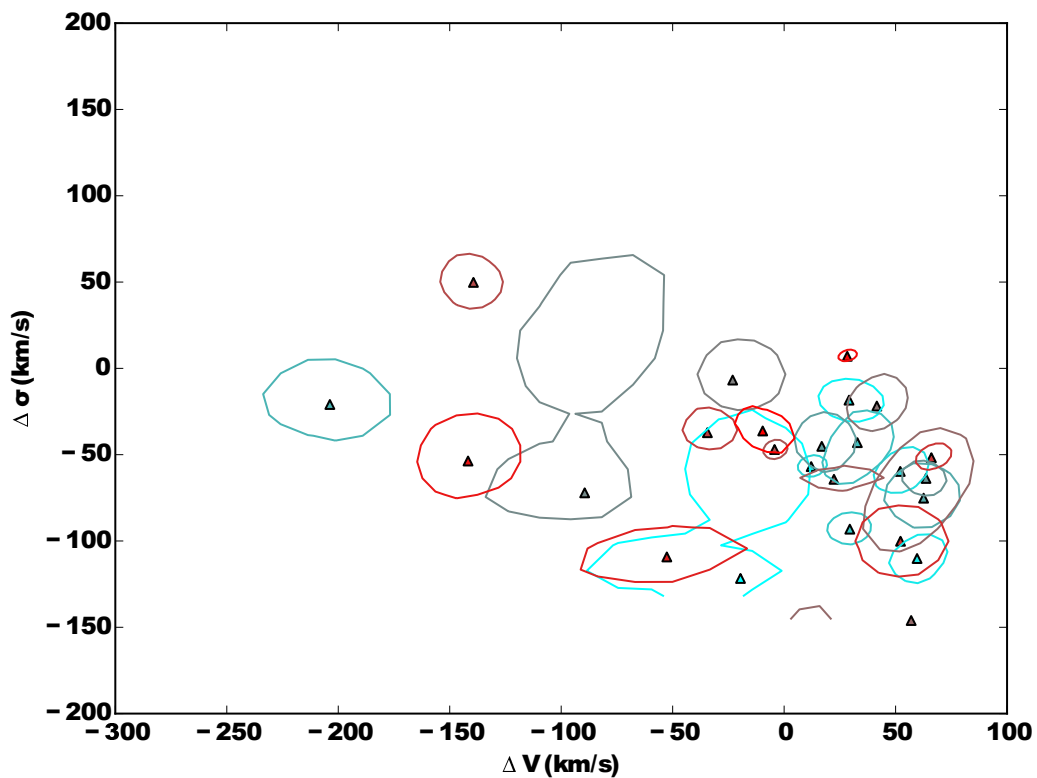
Fig. 4.13 ΔV vs. $\Delta \sigma$ diagrams for Seyferts, from MCMC simulations. The triangles correspond to the position of the 50th percentile in the posterior distribution for the parameters, whereas the contours show the corresponding 68% confidence intervals, for two free parameters. Only in one case of the MCMC simulation did not converge and thus the median value is not within the confidence interval (point at bottom right corner).

Chapter 5

Conclusion

In this thesis we have analysed the SDSS spectra of 963 nearby galaxies, selected for displaying an excessive strength for the Na D 5890,5895Å absorption feature compared to what is expected from photospheric stellar lines, as predicted by standard stellar population models. By carefully re-analysing the spectral region around the Na D lines we have investigated the nature of such absorption excess and obtained its kinematics. Through our analysis we could separate objects where the Na D excess is due to interstellar absorption from those, where, instead, this excess originates, most likely, from an enhancement in the photospheric absorption, which in turn is either due to enhancement in the Na abundance, or a larger fraction of low-mass stars, currently not accounted for by our adopted stellar population models. The lack of reddening by dust and nebular emission further argues against the presence of interstellar Na D absorption in the latter objects. This conclusion is complemented by an Na D excess profiles that are systematically broader than the photospheric Na D lines and that not significantly blue- or red-shifted compared to the galaxy systemic velocity. On the other hand, objects with conspicuous dust reddening and strong emission lines display more varied kinematics for the Na D excess, generally featuring narrower Na D profiles in comparison to the photospheric Na D lines cases, and with a broader range of relative velocities, including a few cases, where outflows are very likely. Finally, drawing from standard classification schemes for the nebular emission displayed by our sample objects, we further investigated in galaxies with true interstellar Na D absorption as to whether the kinematics of the Na D depended on the presence of star-formation or AGN activity.

The main results of this work are as follow:

- Only 6 galaxies among our sample show true interstellar Na D absorption and evidence of strong outflows, where the observed velocity of the Na D excess profile V_{NaD} exceed the intrinsic escape velocity V_{esc}. For spiral galaxies, where a simple

deprojection is possible, mild outflows where at least 16% of the gas is escaping are found in an additional 17 cases.

- Outflows are almost exclusively observed only in galaxies with star-formation or composite star-formation/AGN activity, with only 2 Seyfert nuclei (out of 25, or less than 10%) showing evidence of mild outflows.

- There is no conclusive evidence that the fraction of escaping Na D gas in objects with composite star-forming/AGN activity is boosted as the importance of the AGN component increases.

- In quiescent objects, with no or little, but still undetected nebular emission, we can distinguish objects with broad Na D excess profiles and no reddening by dust. The Na D excess in these galaxies is with some certainty due to template-mismatch, arising from stellar-population effects. For the objects with narrow and slightly blue-shifted Na D excess profiles, with considerable observable reddening by dust, the Na D excess most likely stems of the cold-gas entrained in dust lanes.

- In objects with LINER-like central emission, the Na D excess kinematics shows some resemblance to what is observed for the Na D excess of quiescent objects, pointing also to a mixed contribution of stellar-population effects and of interstellar absorption in dust lanes towards the observed Na D excess. In this context, no distinction could be made between objects, whose LINER-like emission likely originates from true AGN activity, as opposed to those where diffuse ionised-gas emission contributes to their observer spectrum.

While these results certainly cast some doubts on the importance of AGN activity in driving gas outflows in galaxies at the spatial scales of at least a few kpc (as typically subtended by the 3" aperture of the SDSS spectra) and hence on their relevance of AGN feedback for quenching star-formation in the nearby Universe, we need to keep in mind some of the inherent limitations in the Jeong et al. selection from which our sample is drawn. Among these, the most serious drawback of the Jeong et al. sample is that it specifically excluded strongly interacting galaxies and that it was limited to a redshift of 0.08 to allow for a robust morphological classification. This almost certainly had an impact to the number of SDSS galaxies with potentially strong optical AGN activity, that could enter our sample, since in particular Seyfert galaxies are exceedingly rare and tend often to occur in IR-luminous and interacting galaxies.

As a first step to tackle such incompleteness, in Sarzi et al (2016,Appendix A) I contributed towards exploring the incidence of Na D outflows, amongst galaxies that were

preselected only on their likelihood to display radio AGN activity, and could potentially highlight the presence of radio-mode AGN feedback. As it turned out, objects with clear signposts of radio AGN activity are either already devoid of gas or show little to no gas, consistently showing mostly LINER-like emission, either powered by a low-luminosity AGN or by an extended, but rather settled gas system, just like observed in this work. Furthermore, also in this sample objects without radio AGN, but with optical Seyfert activity, showed little or no evidence of Na D outflows as also found here, although in this case the number of Seyferts was rather limited.

In the near future, as a first step into my Ph. D., I intend to try and finally assess the incidence of AGN feedback among Seyfert galaxies in the nearby Universe. For this, I will construct of volume-limited sample of Seyfert galaxies, this time drawn from the entire SDSS survey, irrespective of the likely presence of Na D as done in Jeong et al. Given that Seyfert galaxies amount to 1-2% of the galaxy population, this should still give me approximately 10,000 Seyfert galaxies for which I could investigate the presence of Na D absorption and outflows. The analysis of such a large Seyfert sample, assisted by well-matched control sample in size, absolute-magnitude, morphology and color, should finally help answering whether optical AGN activity is important or not in the outflow budget of the local Universe.

References

Abazajian K. N., et al. 2009, The Astrophysical Journal Supplement Series, 182, 543

Alatalo K., et al. 2011, ApJ, 735, 88

Arav N., Korista K. T., de Kool M., Junkkarinen V. T., Begelman M. C., 1999, ApJ, 516, 27

Baldwin J. A., Phillips M. M., Terlevich R., 1981, PASP, 93, 5

Benson A. J., Bower R. G., Frenk C. S., Lacey C. G., Baugh C. M., Cole S., 2003, ApJ, 599, 38

Blandford R. D., Netzer H., Woltjer L., Courvoisier T. J.-L., Mayor M., eds, 1990, Active Galactic Nuclei

Bruzual G., Charlot S., 2003, Monthly Notices of the Royal Astronomical Society, 344, 1000

Cappellari M., 2013, in Thomas D., Pasquali A., Ferreras I., eds, IAU Symposium Vol. 295, The Intriguing Life of Massive Galaxies. pp 37–44 (arXiv:1210.7742), doi:10.1017/S1743921313004213

Cappellari M., Emsellem E., 2004, PASP, 116, 138

Chabrier G., 2003, PASP, 115, 763

Chen Y.-M., Tremonti C. A., Heckman T. M., Kauffmann G., Weiner B. J., Brinchmann J., Wang J., 2010, AJ, 140, 445

Cid Fernandes R., Stasińska G., Mateus A., Vale Asari N., 2011, MNRAS, 413, 1687

Conroy C., van Dokkum P., 2012a, ApJ, 747, 69

Conroy C., van Dokkum P. G., 2012b, ApJ, 760, 71

Croton D. J., et al. 2006, MNRAS, 365, 11

Davis T. A., et al. 2012, MNRAS, 426, 1574

Erb D. K., 2015, Nature, 523, 169

Everett J. E., 2007, Ap&SS, 311, 269

Fabian A. C., 2012, ARA&A, 50, 455

Ferrarese L., Merritt D., 2000, ApJ, 539, L9

Foreman-Mackey D., Hogg D. W., Lang D., Goodman J., 2013, PASP, 125, 306

Fujita A., Martin C. L., Mac Low M.-M., New K. C. B., Weaver R., 2009, ApJ, 698, 693

Gebhardt K., et al. 2000, ApJ, 539, L13

Genel S., et al. 2014, MNRAS, 445, 175

Heckman T. M., Lehnert M. D., Strickland D. K., Armus L., 2000, ApJS, 129, 493

Ho L. C., 2008, ARA&A, 46, 475

Hobbs L. M., 1973, ApJ, 180, L79

Jefferies J. T., 1968, Spectral line formation

Jenkins E. B., 1986, ApJ, 304, 739

Jeong H., Sukyoung K. Y., Kyeong J., Sarzi M., Sung E.-C., Oh K., 2013, The Astrophysical Journal Supplement Series, 208

Kauffmann G., et al. 2003, MNRAS, 346, 1055

Kewley L. J., Dopita M. A., Sutherland R. S., Heisler C. A., Trevena J., 2001, ApJ, 556, 121

King A., Pounds K., 2015, ARA&A, 53, 115

Kobayashi C., Umeda H., Nomoto K., Tominaga N., Ohkubo T., 2006, ApJ, 653, 1145

Krug H. B., Rupke D. S. N., Veilleux S., 2010, ApJ, 708, 1145

Lehnert M. D., Tasse C., Nesvadba N. P. H., Best P. N., van Driel W., 2011, A&A, 532, L3

Magorrian J., et al. 1998, AJ, 115, 2285

Markwardt C. B., 2009, in Bohlender D. A., Durand D., Dowler P., eds, Astronomical Society of the Pacific Conference Series Vol. 411, Astronomical Data Analysis Software and Systems XVIII. p. 251 (`arXiv:0902.2850`)

Martin C. L., 2005, ApJ, 621, 227

McConnell N. J., Lu J. R., Mann A. W., 2016, ApJ, 821, 39

Morton D. C., 2003, ApJS, 149, 205

Müller-Sánchez F., Prieto M. A., Hicks E. K. S., Vives-Arias H., Davies R. I., Malkan M., Tacconi L. J., Genzel R., 2011, ApJ, 739, 69

Nachman P., Hobbs L. M., 1973, ApJ, 182, 481

Oh K., Sarzi M., Schawinski K., Yi S. K., 2011, ApJS, 195, 13

Peletier R. F., 2013, Stellar Populations. p. 353

Press W. H., Flannery B. P., Teukolsky S. A., 1986, Numerical recipes. The art of scientific computing

Puchwein E., Springel V., 2013, MNRAS, 428, 2966

Rupke D. S., Veilleux S., Sanders D. B., 2002, ApJ, 570, 588

Rupke D. S., Veilleux S., Sanders D. B., 2005a, ApJS, 160, 115

Rupke D. S., Veilleux S., Sanders D. B., 2005b, ApJ, 632, 751

Salpeter E. E., 1955, ApJ, 121, 161

Sarzi M., et al. 2006, MNRAS, 366, 1151

Sarzi M., et al. 2010, MNRAS, 402, 2187

Sato T., Martin C. L., Noeske K. G., Koo D. C., Lotz J. M., 2009, ApJ, 696, 214

Schawinski K., Thomas D., Sarzi M., Maraston C., Kaviraj S., Joo S.-J., Yi S. K., Silk J., 2007, MNRAS, 382, 1415

Schwartz C. M., Martin C. L., 2004, ApJ, 610, 201

Sell P. H., et al. 2014, MNRAS, 441, 3417

Sijacki D., Springel V., Di Matteo T., Hernquist L., 2007, MNRAS, 380, 877

Spiniello C., Trager S. C., Koopmans L. V. E., Chen Y. P., 2012, ApJ, 753, L32

Spitzer Jr. L., 1948, ApJ, 108, 276

Spitzer L., 1968, Diffuse matter in space

Spitzer L., 1978, Physical processes in the interstellar medium

Spitzer Jr. L., Lautman D. A., 1956, ApJ, 123, 363

Strömgren B., 1948, ApJ, 108, 242

Veilleux S., Cecil G., Bland-Hawthorn J., 2005, ARA&A, 43, 769

White S. D. M., Rees M. J., 1978, MNRAS, 183, 341

Zieleniewski S., Houghton R. C. W., Thatte N., Davies R. L., 2015, MNRAS, 452, 597

van Dokkum P. G., 2008, ApJ, 674, 29

Appendix A

Cold-gas outflows in typical low-redshift galaxies are driven by star formation, not AGN

MarcSarzi[1], Sugata Kaviraj[1], Borislav Nedelchev[1], Joshua Tiffany[2], Stanislav S. Shabala[3], Adam T. Deller[4] and Enno Middelberg[5]

[1]Centre for Astrophysics Research, University of Hertfordshire, College Lane, Hatfield AL10 9AB, United Kingdom

[2]Astronomy Unit, School of Physics and Astronomy, Queen Mary University of London, London E1 4NS, UK

[3]School of Mathematics and Physics, University of Tasmania, Private Bag 37, Hobart, TAS 7001, Australia

[4]The Netherlands Institute for Radio Astronomy (ASTRON), Dwingeloo, The Netherlands

[5]Astronomisches Institut der Ruhr-Universitat Bochum, Universitatsstrae 150, D-44801 Bochum, Germany

A.1   Introduction

Understanding the processes that quench star formation activity is key to following how galaxies evolve over cosmic time. In massive galaxies, which have deep potential wells, the current view is that stellar winds and supernovae explosions are not powerful enough to eject gas and regulate star formation (e.g., Silk & Rees 1998). Instead, this quenching is

typically attributed to a central active galactic nucleus (AGN, e.g., Croton et al. 2006; Shabala & Alexander 2009), because the energy released by the growth of the black hole can be orders of magnitude larger than the binding energy of the gas, even in the most massive systems (e.g., Fabian 2012). Observational evidence for this process remains mixed, however. While some examples of AGN-driven outflows do exist both at high and low redshifts (e.g., Nesvadba et al. 2008; Nyland et al. 2013, respectively), it is unclear whether gas outflows are routinely driven by AGNs. In particular, recent work at low redshift indicates that the onset of the AGN appears to lag behind the peak of the starburst by several dynamical timescales (Kaviraj 2009; Wild, Heckman & Charlot 2010; Shabala et al. 2012; Kaviraj et al. 2015b), which implies that the gas reservoir has been significantly depleted before the AGN had a chance to couple to it. To probe this issue in more detail, it is desirable to investigate whether signatures of cold-gas outflows exist in systems that host optical or radio AGNs and to see how these outflows compare to those in star-bursting systems.

An effective way of carrying out this exercise is to explore the presence of interstellar Na I $\lambda\lambda 5890, 5895$ (NaD) absorption in nearby galaxies. When outflows occur in galaxies, neutral material entrained in the flow can be observed against the stellar background via characteristic absorption lines (e.g., Rupke, Veilleux, & Sanders 2005; Sato et al. 2009; Chen et al. 2010), particularly in systems with low inclination. At optical wavelengths, the strongest of such absorption lines are produced by neutral Sodium and observed via the NaD doublet. Thus, if AGN feedback routinely shuts down star formation by driving cold-gas outflows, one expects to find an excess of NaD absorption over what is expected from stellar photospheres alone, which is blueshifted compared to the position of the photospheric NaD lines.

In this Letter, we use optical spectra from the Sloan Digital Sky Survey (SDSS, Abazajian et al. 2009) to investigate the NaD properties of a sample of galaxies that have been observed by the mJy Imaging VLBA Exploration at 20 cm survey (Deller & Middelberg 2014, hereater mJIVE-20). While SDSS spectra enable us to identify optical AGNs, the sub-arcsecond radio imaging obtained with the Very Long Baseline Array (VLBA) during the mJIVE-20 survey allows us to unequivocally identify the presence of radio AGN activity. Taken together, these data enable a detailed exploration of whether AGN are an important driver of outflows in the massive galaxy population.

This paper is organised as follows. In § A.2 we describe our sample together with the mJIVE-20 survey and SDSS data that underpin this study, whereas § A.3 describes our analysis of the NaD absorption lines. In § A.4 we then scrutinise the kinematics of the NaD lines to robustly identify objects with interstellar NaD absorption and look for evidence for starburst- or AGN-driven cold-gas outflows. Finally, we draw our conclusions in § A.5.

Morph. / em.-line class	all objects		mJIVE-20 det.	
	all	with NaD	all	with NaD
ETG / SF	19	6	1	0
ETG / TO	15	6	4	1
ETG / Sy	19	4	3	0
ETG / LI	9	4	5	2
ETG / NE	204	42	80	15
LTG / SF	69	29	0	0
LTG / TO	46	26	2	0
LTG / Sy	26	9	1	0
LTG / LI	9	3	3	1
LTG / NE	27	16	0	0
Merger / SF	4	1	0	0
Merger / TO	0	0	0	0
Merger / Sy	3	0	2	0
Merger / LI	2	0	1	0
Merger / NE	4	2	1	1

Table A.1 Breakdown of our sample according to galaxy morphology and nebular emission classification (where NE stands for objects with little or no emission), for all our objects and those with a VLBI radio core, as well as for those with detected NaD excess.

A.2 Sample and Data

Our sample comprises of galaxies observed during the mJIVE-20 survey for which images and spectra are available from the SDSS. mJIVE-20 is a survey that systematically observed objects detected by the Faint Images of the Radio Sky at Twenty cm (FIRST, Becker, White & Helfand 1995), with a median detection threshold of 1.2 mJy/beam and a typical beam size of $\sim 0.''01$ that effectively allows to zoom in on the FIRST targets to further study the nature of the radio emission and ascertain in particular the presence of a radio core associated with an AGN. The mJIVE-20 survey has targeted $\sim$25,000 FIRST sources, with ~ 5000 very-long baseline interferometry (VLBI) detections.

We cross-matched the mJIVE-20 targets with the DR7 value-added SDSS catalogue of Oh et al. (2011, hereafter OSSY), since this contains spectral measurements for the stellar kinematics and the nebular emission within the 3" SDSS fiber. Based on `pPXF` and `GandALF` fits (Cappellari & Emsellem 2004; Sarzi et al. 2006), the OSSY catalogue also provides us with a measurement for the level of detection of the emission lines through their A/N ratio, between the peak amplitude of the lines and noise level in the `GandALF` fit residuals, and a gauge for the amount of dust extinction that affects the entire SDSS spectrum. Such a diffuse E(B-V) measurement is particularly relevant to this work, since

it corresponds well to the presence of interstellar NaD absorption (Jeong et al. 2013). The OSSY database also readily provides us with the best-fitting model for the stellar continuum, which is central to correctly characterise the extent and kinematics of interstellar NaD absorption. Finally, the OSSY catalogue is restricted to targets at $z < 0.2$ so that a robust visual classification of the galaxy morphology is possible.

Overall, our sample includes 456 galaxies with a median stellar mass of $10^{11} M_\odot$. Of these, 58% are early-type galaxies (ETGs), 39% are spirals (LTGs) and 3% are on-going mergers. Approximately 23% of our sample (103 galaxies) have VLBI detections, 90% of which occur in ETGs. Tab. A.1 provides a breakdown of our sample according to galaxy morphology and to whether they have a VLBI radio core.

A.3 Spectral Analysis

In order to assess the presence of interstellar NaD absorption and measure the kinematics of such absorbing clouds, we follow the approach of Rupke, Veilleux, & Sanders (2005) after normalising the SDSS spectra for the best-fitting stellar continuum provided by the OSSY catalogue. We assume a single Maxwellian velocity distribution for the absorbers along the line of sight and that the covering fraction C_f of such clouds is itself independent of velocity. Under these assumptions the absorption profile of the interstellar NaD lines can be written as

$$I(\lambda) = 1 - C_f \left\{ 1 - \exp \left[-2\tau_0 e^{-(\lambda-\lambda_{\rm blue})^2/(\lambda_{\rm blue}b/c)^2} - \tau_0 e^{-(\lambda-\lambda_{\rm red})^2/(\lambda_{\rm red}b/c)^2} \right] \right\} \quad (A.1)$$

where $\lambda_{\rm blue}$ and $\lambda_{\rm red}$ are the redshifted central wavelength of the Na I doublet, τ_0 is the optical depth at the centre of the red line, and $b = \sqrt{2}\sigma$ is the Doppler parameter that measures the width of the lines. This parametrisation thus yield a measurement for the velocity $V_{\rm NaD}$ and width $\sigma_{\rm NaD}$ of the NaD lines, as well as the optical depth τ_0 and covering factor C_f of the absorbing clouds.

After normalising the SDSS spectra of our sample galaxies for the OSSY continuum model we proceed to fit with the Rupke, Veilleux, & Sanders method any possible excess of NaD absorption in the data compared to what is expected from the photospheric absorption provided by the OSSY best fitting stellar-population model. Our approach implicitly assumes that any NaD absorption excess is due to interstellar absorption but in fact this is not always the case. Indeed, ETGs showing little or no dust absorption in their images or nebular emission in their spectra often exhibit an NaD excess that is most likely due to an enhanced [Na/Fe] abundance in their stellar populations that cannot be accounted for by most
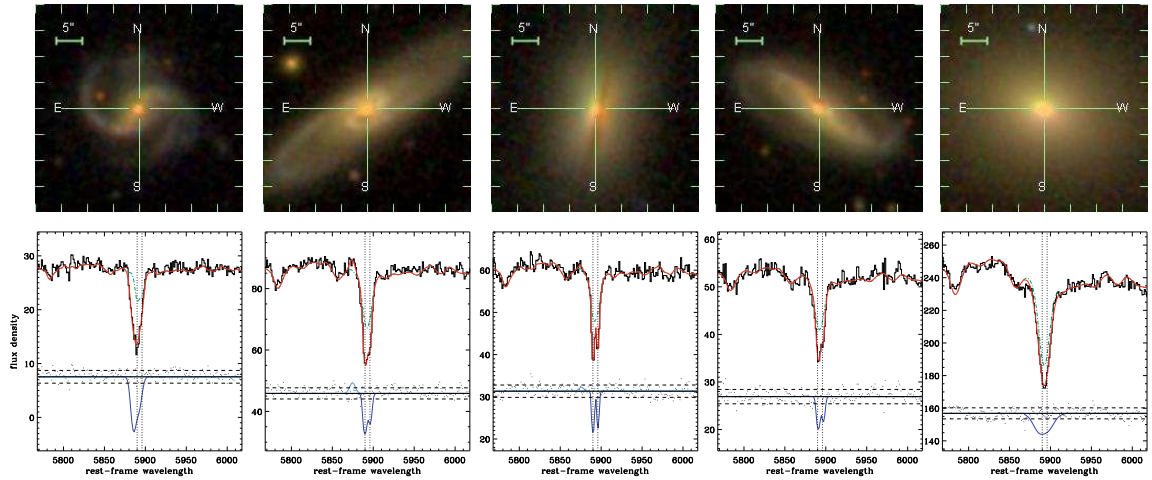
Fig. A.1 SDSS colour images (top row) and spectral fits in the NaD region (bottom row) for five of our sample galaxies. In the lower panels the red line shows our best-fitting model, which is a superposition of our best `GandALF` fit to the stellar continuum and nebular emission across the entire spectrum (green dashed and cyan lines, respectively) and of our fit to the NaD absorption excess using the formalism of Rupke, Veilleux, & Sanders (2005, blue line, see § A.3). The residuals of our fit (black dots) have been rescaled by adding a constant (marked by the horizontal lines), and their standard deviation (horizontal dashed lines) is used to assess the level of detection of the NaD excess features. The vertical dotted lines mark the rest-frame position of the NaD lines.

stellar population models (Jeong et al. 2013), in particular given that in such smooth and ordinary ETGs the NaD excess shows little or no kinematic offset compared to the systemic velocity (Park, Jeong and Yi 2015). However, in what follows, we will show that objects where the NaD excess stems from template mismatch can be clearly isolated in terms of both the position and width of their best-fitted NaD profile in addition to their reddening and nebular properties.

Fig. A.1 shows SDSS colour images and our spectral fit in the NaD region for five galaxies in our sample, all of which display a significant excess of NaD absorption compared to the photospheric NaD absorption of the best-fitting stellar-population model (i.e., the A/N ratio for the fitted NaD profile is < -3). Fig. A.1 also indicates the different nature of the NaD absorption excess between spiral or dusty ETGs and quiescent objects. Indeed, whereas in spiral galaxies and dust-lane ellipticals our fit returns narrow NaD profiles that can be either blue- or even slightly redshifted (first four panels from the left), the NaD excess of quiescent ETGs (rightmost panel) is generally characterised by rather broad NaD model profiles. Tab. A.1 also specifies where NaD excess occurs in our sample.
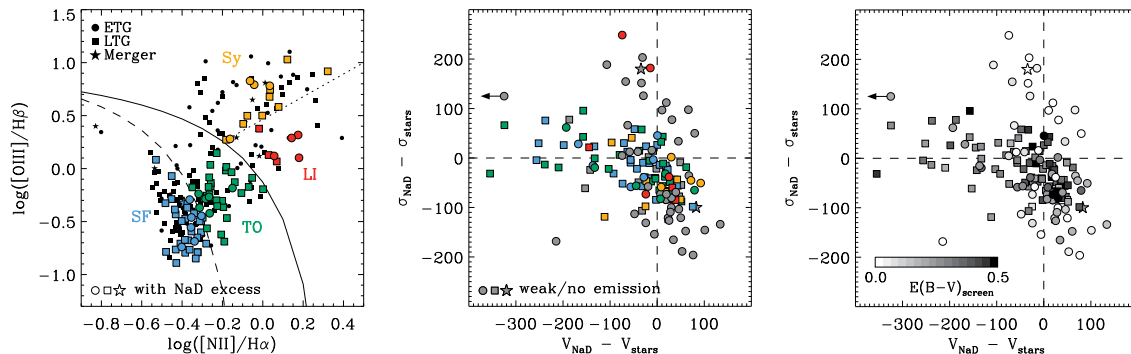
Fig. A.2 Emission-line classification and NaD kinematic properties of our sample galaxies. Left: [N II]/Hα vs. [O III]/Hβ BPT diagram for mJIVE-20 targets with noticeable nebular emission (i.e., with A/N > 3 in all four lines). The shape of the symbols shows the galaxy morphology, whereas coloured symbols highlight objects with significant NaD absorption excess (i.e., with A/N for NaD < −3) and their emission-line classification. The dashed, solid and dotted lines showing the boundary between objects with star-forming, composite, Seyfert and LINER emission are from Kauffmann et al. (2003), Kewley et al. (2001) and Schawinski et al. (2007), respectively. Middle and right: $V_{\rm NaD} - V_{\rm stars}$ vs. $\sigma_{\rm NaD} - \sigma_{\rm stars}$ velocity and velocity dispersion offset diagrams, showing the kinematic properties of the NaD lines for objects that show a significant NaD absorption excess. In the middle panel the symbols are colour-coded according to the emission-line classification or are shown in grey if nebular emission was weak or absent. In the right panel darker shades of grey for the symbols correspond to increasing amounts of reddening by dust (affecting the entire SDSS spectra). Objects with significant amount of dust extinction display an NaD kinematics consistent with outflows (for negative $V_{\rm NaD} - V_{\rm stars}$ values), settled dusty disks (with narrower interstellar NaD line profiles w.r.t stellar absorption features), and possibly also mild inflows. On the other hand, in galaxies without much reddening any NaD excess is more likely associated to template-mismatch effects, and these objects tend to show rather large $\sigma_{\rm NaD} - \sigma_{\rm stars}$ values.

A.4   Results

A.4.1   Entire Sample

We begin by discussing the emission-line classification and, where present, the properties of the NaD excess for our entire sample. Fig. A.2 (left panel) shows the standard Baldwin, Phillips & Terlevich (1981, BPT) diagnostic diagram that juxtaposes the [O III]/Hβ and [N II]/Hα line ratios (Veilleux & Osterbrock 1987) for objects with A/N> 3 for all four lines, from which we deduce their emission-line class. Of the 221 objects that are in this BPT diagram, which are nearly 48% of the sample (see also Tab. A.1), most show emission either dominated by star-forming regions (hereafter SF, 42% of active objects) or by the
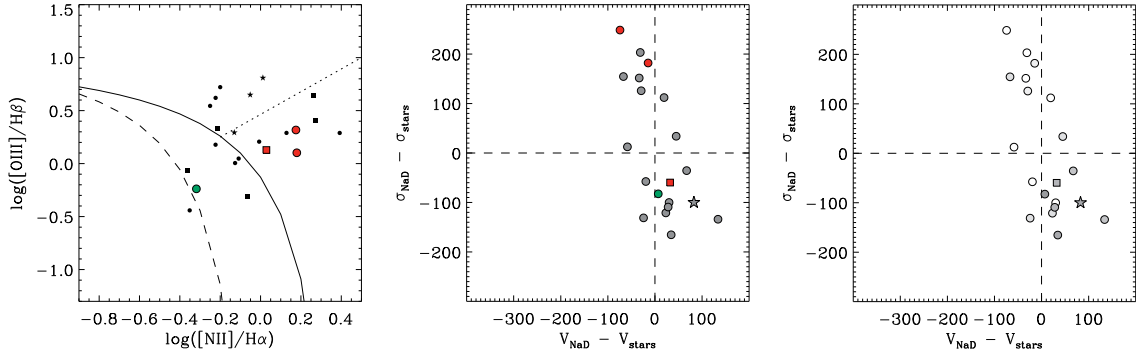
Fig. A.3 Same as Fig. A.2 but now only for objects with detected radio cores in the mJIVE-20 survey. These are predominantly quiescent or weakly emitting early-type galaxies with NaD excess due either to the presence of settled disks and dust lanes, or which is induced by template-mismatch.

likely superposition of star-bursting and AGN activity (TO for "transition objects", 28%), with the remaining objects exhibiting either Seyfert activity (Sy, 22%) or central LINER emission (LI, 9%). The remaining 235 objects in our sample (nearly 52%) display only weak (e.g., with only Hα and [N II] detected emission) or no nebular emission, which is puzzling considering that only 1/3 of these objects show a compact radio core at VLBI resolution so that radio AGN activity could account for their FIRST radio flux. On the other hand, since 87% of such quiescent or weakly emitting objects are ETGs, it is likely that for many of those without a VLBI detection the FIRST radio flux is due to circumnuclear or rather extended star-formation activity, which would add to existing evidence of recent star-formation in many ETGs based on UV imaging (e.g., Yi et al. 2005; Jeong et al. 2007).

Moving on with the properties of the NaD absorption excess for our entire sample, the middle and right panels of Fig. A.2 show - for objects where such an absorption excess is detected - how the position and width of our best-fitting NaD profile compares to that of the stellar line-of-sight velocity distribution. In these $V_{NaD} - V_{stars}$ vs. $\sigma_{NaD} - \sigma_{stars}$ diagrams we can identify objects with a) possible NaD outflows where $\Delta V \leq -100\,km\,s^{-1}$, b) relaxed dusty disks where $\Delta V \sim 0$ but $\Delta\sigma < 0$, corresponding to narrower NaD interstellar absorption lines compared to stellar photospheric features, c) possible mild inflows due to bars or unsettled dust lanes where $\Delta\sigma < 0$ and $\Delta V > 0$, and finally d) systems that systematically show $\Delta\sigma > 0$, $\Delta V \sim 0$ and no evidence for an interstellar medium as their `GandALF` fits imply little or no need for reddening by dust (Fig. A.2, right panel) and only weak or no nebular emission. The NaD excess of these last objects is almost certainly due to template-mismatch, where the large width of such an excess is likely driven by an enhanced

presence of cool stars and the strong pressure-broadened wings of their NaD photospheric lines.

There are 23 objects with possible NaD outflows in our sample, most of which (74%) exhibit either SF or TO central activity, consistent with SDSS studies on starburst-driven outflows (e.g., Chen et al. 2010) and possibly with an evolution from starburst to quenched galaxies with star formation decreasing along this path as AGN emerge (e.g., Yesuf et al. 2014), respectively. On the other hand, there is little evidence for NaD outflows in galaxies harbouring Seyfert nuclei or LINER emission. The few objects with little or no nebular emission that show evidence of NaD outflow in Fig.A.2 (including a spectacular case with $\Delta V \sim -1000\,\mathrm{km\,s^{-1}}$ shown by the left-pointing arrow) are most likely SF or TO where the [O III] line remained undetected due to large amounts of reddening.

A.4.2   mJIVE-20 Detected Objects

Around 23% of our FIRST-selected sample of galaxies (103 objects) show unequivocal signatures of AGN activity through to the detection of a compact radio core in the mJIVE-20 images. These are generally (79% of the cases) objects that show only weak or no nebular emission, or which are otherwise evenly distributed between the regions of the [O III]/Hβ vs. [N II]/Hα BPT diagram that include transition objects, Seyfert nuclei and galaxies with LINER emission, consistent with the presence of an AGN as signalled by the finding of a compact radio core. In fact, central SF activity in our VLBI-detected objects is likely to be rather limited given that most of their FIRST flux is unresolved (90 objects have more than 80% of their total FIRST flux density in an unresolved component) and that generally (86 objects, or 83%) more than half of this compact emission is found in the VLBI component. Furthermore, VLBI-detected galaxies reside primarily on the red-sequence of passively-evolving system in the UV-optical color-magnitude diagram (Kaviraj et al. 2015a), which is sensitive to even small fractions of young stars (Yi et al. 2005; Kaviraj et al. 2007).

Among the VLBI-detected objects, 20 ($\sim 19\%$) show an NaD absorption excess, and these are predominantly ETGs with little or weak nebular emission (Fig. A.3). For a third of these galaxies, however, such an excess is most likely induced by template-mismatch given their position in the $V_{\mathrm{NaD}} - V_{\mathrm{stars}}$ vs. $\sigma_{\mathrm{NaD}} - \sigma_{\mathrm{stars}}$ diagram and their lack of reddening by dust. The remaining objects, a dozen at best, show no evidence of outflows and are instead consistent with the presence of relaxed dusty disks or slight inflows, possibly indicating unsettled dust-lanes. Thus, only a minority of nearby radio AGN is found in galaxies where NaD absorption indicates the presence of cold-gas, and in no systems do we find evidence for such a medium to be outflowing.

This result contrasts with the findings of Lehnert et al. (2011), who detected an NaD excess in approximately 1/3 of their sample of radio-loud ETGs and with NaD profiles showing little or no kinematic offset ($\Delta V \sim -50\,\mathrm{km\,s^{-1}}$) but very broad profiles ($\sigma_{\mathrm{NaD}} \sim 500\,\mathrm{km\,s^{-1}}$). Part of this discrepancy may be due to differences in sample selection. Lehnert et al. analysed a sample of 700 radio-loud ETGs at $z < 0.2$, with FIRST 1.4 GHz flux densities above 40 mJy and resolved jet morphologies. This selection would naturally sample high-density environments such as galaxy clusters where a hot-gas medium is available for the AGN to work against and produce detectable radio lobes. On the other hand, the mJIVE-20 survey is capable of detecting compact radio AGN regardless of local environment and thus probes AGNs in the general galaxy population that largely inhabits relatively low-density environments (Kaviraj et al. 2015a). The working of radio AGN activity may thus be different in these two samples, being directly fuelled by the cooling of hot gas in cluster centres in the former (Hardcastle, Evans, & Croston 2007; Shabala et al. 2008) while being triggered by minor mergers in the latter (Best & Heckman 2012; Kaviraj et al. 2015a). Additionally, it may be that also some of the NaD excess detected by Lehnert et al. is induced by template-mismatch, in particular given than the limitations of stellar-population models are most evident in massive ETGs such as central cluster galaxies. In fact, it is only in the most massive ETGs of our sample (with $\sigma_{\mathrm{star}} \sim 250\,\mathrm{km\,s^{-1}}$) that we find NaD excess due to template-mismatch, with NaD profiles as wide (up to $\sigma_{\mathrm{NaD}} \sim 500\,\mathrm{km\,s^{-1}}$) as those observed by Lehnert et al..

A.5   Conclusions

Using the NaD interstellar absorption as a tracer of neutral gas we have looked for cold-gas outflows in a sample of 456 nearby galaxies with known central radio-continuum emission from the FIRST survey and for which we could unambiguously ascertain the presence of nuclear radio activity using our mJIVE-20 radio imaging at milli-arcsecond scales. VLBI-detected radio cores are found in approximately 23% of our sample (103 objects) and occur predominantly in early-type galaxies with little or no nebular emission in their SDSS spectra and which are dominated by old stellar populations. Only in a dozen objects such radio AGN activity is accompanied by interstellar NaD absorption, but the neutral gas traced by the NaD lines never appears to be outflowing. On the other hand, interstellar NaD absorption is detected in 1/3 of the objects that do not possess a VLBI radio core (in 122 out 353 objects), consistent with the presence of a conspicuous gaseous medium where most of the time star formation contributes significantly to their central FIRST radio emission. Only in

such objects - without a radio AGN - do we find evidence of cold-gas outflows, and these generally arise in spiral galaxies with central SF or TO nebular activity.

These findings reinforce the picture in which radio AGN activity occurs most often in systems where the gas reservoir has already been significantly depleted. Interestingly, across our entire sample cold-gas outflows occur only in objects dominated by central starburst or composite AGN/star-formation activity whereas optical Seyfert AGN activity does not seem capable of driving such winds. This result suggests either that only supernovae feedback can drive galactic winds in the objects that we have studied or that the role of optical AGN activity in this respect is limited to a phase accompanied by significant star-formation activity.

Acknowledgements

References

Abazajian K. N., et al., 2009, ApJS, 182, 543

Baldwin, J. A., Phillips, M. M., Terlevich, R. 1981, PASP, 93, 5

Becker R. H., White R. L., Helfand D. J., 1995, ApJ, 450, 559

Best P. N., Heckman T. M., 2012, MNRAS, 421, 1569

Cappellari M., Emsellem E., 2004, PASP, 116, 138

Chen Y.-M., Tremonti C. A., Heckman T. M., Kauffmann G., Weiner B. J., Brinchmann J., Wang J., 2010, AJ, 140, 445

Croton D. J., et al., 2006, MNRAS, 365, 11

Deller A. T., Middelberg E., 2014, AJ, 147, 14

Fabian A. C., 2012, ARA&A, 50, 455

Jeong H., Bureau M., Yi S. K., Krajnović D., Davies R. L., 2007, MNRAS, 376, 1021

Jeong H., Yi S. K., Kyeong J., Sarzi M., Sung E.-C., Oh K., 2013, ApJS, 208, 7

Hardcastle M. J., Evans D. A., Croston J. H., 2007, MNRAS, 376, 1849

Kauffmann G., et al., 2003, MNRAS, 346, 1055

Kaviraj S., et al., 2007, ApJS, 173, 619

Kaviraj S., 2009, MNRAS, 394, 1167

Kaviraj S., Shabala S. S., Deller A. T., Middelberg E., 2015a, MNRAS, in press, arXiv:1412.5602

Kaviraj S., Shabala S. S., Deller A. T., Middelberg E., 2015b, MNRAS, 452, 774

Kewley L. J., Dopita M. A., Sutherland R. S., Heisler C. A., Trevena J., 2001, ApJ, 556, 121

Lehnert M. D., Tasse C., Nesvadba N. P. H., Best P. N., van Driel W., 2011, A&A, 532, L3

Nesvadba N. P. H., Lehnert M. D., De Breuck C., Gilbert A. M., van Breugel W., 2008, A&A, 491, 407

Nyland K., et al., 2013, ApJ, 779, 173

Oh K., Sarzi M., Schawinski K., Yi S. K., 2011, ApJS, 195, 13

Park, J., Jeong H., Yi S. K., 2015, ApJ, in press, arXiv:1507.03342

Rupke D. S., Veilleux S., Sanders D. B., 2005, ApJS, 160, 87

Sarzi M., et al., 2006, MNRAS, 366, 1151

Sato T., Martin C. L., Noeske K. G., Koo D. C., Lotz J. M., 2009, ApJ, 696, 214

Schawinski K., Thomas D., Sarzi M., Maraston C., Kaviraj S., Joo S.-J., Yi S. K., Silk J., 2007, MNRAS, 382, 1415

Shabala S. S., Ash S., Alexander P., Riley J. M., 2008, MNRAS, 388, 625

Shabala S., Alexander P., 2009, ApJ, 699, 525

Shabala S. S., et al., 2012, MNRAS, 423, 59

Silk J., Rees M. J., 1998, A&A, 331, L1

Veilleux, S., Osterbrock, D. E. 1987, ApJS, 63, 295

Wild V., Heckman T., Charlot S., 2010, MNRAS, 405, 933

Yesuf H. M., Faber S. M., Trump J. R., Koo D. C., Fang J. J., Liu F. S., Wild V., Hayward C.'C., 2014, ApJ, 792, 84

Yi S. K. et al. 2005, ApJ, 619, L111